Neuroscience
Physics of Living Systems

A Deep Learning Pipeline for Mapping in situ Network-level Neurovascular Coupling in Multi-photon Fluorescence Microscopy

Matthew Rozak, **James Mester**, **Ahmadreza Attarpour**, **Adrienne Dorr**, **Maged Goubran**, **Bojana Stefanovic**

Department of Medical Biophysics, University of Toronto, Toronto, Ontario, Canada • Physical Sciences, Sunnybrook Research Institute, Toronto, Ontario, Canada • Hurvitz Brain Sciences, Sunnybrook Research Institute, Toronto, Ontario, Canada

Reviewed Preprint

Published from the original preprint after peer review and assessment by eLife.

About eLife's process

Reviewed preprint version 1
April 3, 2024 (this version)

Posted to preprint server
January 24, 2024

Sent for peer review
January 24, 2024

Abstract

1 Abstract

Functional hyperaemia is a well-established hallmark of healthy brain function, whereby local brain blood flow adjusts in response to a change in the activity of the surrounding neurons. Although functional hyperemia has been extensively studied at the level of both tissue and individual vessels, vascular network-level coordination remains largely unknown. To bridge this gap, we developed a deep learning-based computational pipeline that uses two-photon fluorescence microscopy images of cerebral microcirculation to enable automated reconstruction and quantification of the geometric changes across the microvascular network, comprising hundreds of interconnected blood vessels, pre and post-activation of the neighbouring neurons. The pipeline's utility was demonstrated in the Thy1-ChR2 optogenetic mouse model, where we observed network-wide vessel radius changes to depend on the photostimulation intensity, with both dilations and constrictions occurring across the cortical depth, at an average of 16.1±14.3 μm (mean±stddev) away from the most proximal neuron for dilations; and at 21.9±14.6 μm away for constrictions. We observed a significant heterogeneity of the vascular radius changes within vessels, with radius adjustment varying by an average of 24 ± 28% of the resting diameter, likely reflecting the heterogeneity of the distribution of contractile cells on the vessel walls. A graph theory-based network analysis revealed that the assortativity of adjacent blood vessel responses rose by 152 ± 65% at 4.3 mW/mm^2 of blue photostimulation *vs.* the control, with a 4% median increase in the efficiency of the capillary networks during this level of blue photostimulation in relation to the baseline. Interrogating individual vessels is thus not sufficient to predict how the blood flow is modulated in the network. Our computational pipeline, to be made openly available, enables tracking of the microvascular network geometry over time, relating caliber adjustments to vessel wall-associated cells' state, and mapping network-level flow distribution impairments in experimental models of disease.

eLife assessment

This **valuable** work describes a highly complex automated algorithm for analyzing vascular imaging data from two-photon microscopy. This tool has the potential to fill gaps in knowledge of hemodynamic activity across a regional network. The underlying methods and results are still **incomplete**; the biological application provided has several problems that make many of the scientific claims in the paper questionable and the generalizability of the pipeline needs to be further addressed. We believe these concerns could be addressed.

2 Introduction

To support healthy brain functioning, the cerebrovascular network undergoes continual adjustments in vessel calibers [1]–[3]. Neurovascular coupling refers to the change in blood flow following changes in the level of neuronal activity: under physiological conditions, a generous buffer of nutrients is granted to activated parenchyma via the capillary network [1], [4]. This buffer is maintained through finely tuned regulation of flow through changes in the vessel caliber, mediated via contractile cells in the vessel walls. In the absence of such tuning, pockets of tissue could experience inadequate access to metabolites [5]. Alterations in smooth muscle cells, pericytes, and astrocytes may lead to compromises in vessels' dilatory capacity and thus deficits in neurovascular coupling [6]–[9]. In various brain pathologies, including Alzheimer's disease, stroke, and trauma, regional blood flow regulation gets impaired through vessel loss and/or dysfunction of the vessels' dilatory capacity, resulting in regions of ischemia/hypoxia [10], [11]. Previous studies have examined either individual vessels or the tissue level responses, with little attention having been paid to the vascular network, though network dysfunction frequently is associated with accelerated disease progression and long-term symptomatology [3], [12]–[20].

While there is copious data on the functioning of individual vessels, interrogation of the microvascular network remains a challenge, in terms of both data acquisition and analysis [6], [7], [21]–[23]. To date, studies on the brain vasculature have been done by sparsely imaging individual blood vessels at the cellular scale [6], [7], [21], [24]–[32], thereby severely undersampling the microvascular network; or by evaluating the averaged flow over many vessels at the mesoscopic scale, thus failing to discern the flow through individual vessels. A critical gap in the field is the characterization of flow across hundreds of individual vessels, while imaging the network structure that links them together to determine how the vascular response is coordinated across the network. This gap is particularly significant as studies investigating blood flow across several vessels at a time (imaged by varying the line acquisition pattern [6], [24]) have shown highly heterogeneous responses among capillaries. Neuronal function impairments arise wherever local metabolite supply becomes inadequate, notwithstanding the physiological level of flow across the network as a whole, making mapping of vessel changes across the network of particular importance.

To address the limitations of previous work, we developed a novel deep learning (DL)-based pipeline for mapping changes to the geometry of the brain vascular network following neuronal activation, from a time series of volumetric two-photon fluorescence microscopy (2PFM) data. Neuronal activation was elicited by photostimulation of pyramidal neurons expressing Channelrhodopsin-2 (ChR2) [33] in the Thy1-ChR2-YFP mouse model [34]. Our DL pipeline enabled automatic and accurate segmentation, registration and network analysis of large 2PFM datasets across time. We applied our pipeline in a dataset of 17 Thy1-ChR2-YFP mice to map

photostimulation-induced changes across the microvascular network - at the level of individual vessels and at the level of vertices spaced every micrometre along the vessels – in relation to the distance to the closest pyramidal neurons expressing the optogenetic actuator and across the cortical depth. Our findings demonstrate the utility of our pipeline for studying in situ microvascular morphology and function to address various neuroscientific hypotheses.

3 Methods

3.1 Cohort

Animals

All experimental procedures in this study followed the ARRIVE 2.0 guidelines [35]. They were approved by the Animal Care Committee of the Sunnybrook Research Institute, which adheres to the policies and guidelines of the Canadian Council on Animal Care and meets all the requirements of the Provincial Statute of Ontario, Animals for Research Act, and the Canadian Federal Health of Animals Act. We used 15 male and 13 female Thy1-ChR2-YFP mice (#007612, line 18, Jackson Laboratory) at 6-12 months of age (283.9 ± 67.0 days), weighing 28.8±7.1g on the day of imaging. The mice were bred in-house and housed under a 12-hr light/dark cycle [34]. In this mouse line, Channelrhodopsin-2 is expressed preponderantly by pyramidal neurons with soma in cortical layer 5 and dendrites projecting to the cortical surface, enabling depolarization of their cellular membranes and action potential generation upon blue light illumination [30], [34]. An attrition schematic is provided in **Supplementary Figure 1**.

Surgical Preparation

On the day of imaging, mice were induced with 5% isoflurane, transferred to a rectal probe feedback-regulated heating pad (CWE Inc, Ardmore PA) to maintain a temperature of 37 °C, and maintained under 2% isoflurane. A subcutaneous injection of 1 mL of lactated Ringer's solution was administered at the start of surgery. Throughout the surgical preparation and imaging, we monitored breath rate, heart rate, arterial blood oxygen saturation, pulse distention, and breath distention via a pulse oximeter, with a probe mounted on the thigh (MouseOx, STARR Life Sciences) (**Supplementary Table 1**). For fine control over respiration, the mice were tracheostomized with an endotracheal tube (20 Ga catheter) and ventilated with a gas mixture of 20-30% O_2 and medical air using a small animal ventilator (SAR 830/P, CWE Inc, Ardmore PA) set to 115-130 breaths per minute at an inspiratory/expiratory ratio of 1:3-4. Their heads were immobilized via ear bars during the placement of the cranial window and imaging. The tail vein was cannulated with a 26 Ga catheter to enable fluorophore and anesthetic delivery. A cranial window was implanted over the forelimb region of the primary somatosensory cortex (AP 0.25mm, ML 2.0 mm); the dura was excised, and 1% agarose was applied between the brain and the glass coverslip. A well was built using dental cement to allow water immersion of the objective. Texas Red dextran (70 kDa MW, Thermo Fisher Scientific Inc, Waltham MA) was diluted in PBS and injected through the tail vein catheter at a concentration of 33 mg/kg for a total injection volume between 0.1 and 0.2 mL. A line containing 0.01 g/ml alpha chloralose was connected to the tail vein catheter. The animal was then positioned underneath the microscope objective, and the structural 2PFM scan acquired, as detailed below. Seventeen mice (nine male and eight female) made it through the surgical preparation (cf. **Supplementary Figure 1**). Following the structural acquisition, the isoflurane was discontinued, and the continuous infusion of alpha chloralose commenced at 40 mg/kg/hr.

3.2 Imaging

Two-photon Fluorescence Imaging and Optogenetic Stimulation

Mice were imaged on an FVMPE-RS microscope (Olympus, Japan) using a 25x/1.05NA objective. An Insight tunable Ti:Saphire near-infrared laser (SpectraPhysics, USA) was used for 900 nm excitation of Texas Red-labelled vasculature and YFP-labeled ChR2-expressing pyramidal neurons. Two visible light stimulation lasers were used to excite ChR2 at either 458 nm or 552 nm (control). The optical setup is shown in **Figure 1**. The imaging field-of-view was selected to include at least one penetrating artery and vein yet avoid major pial vessels and thus signal loss in the underlying cortex. Structural scans were acquired under 2% isoflurane using a Galvano scanner, with 2x averaging, a z-step of 0.99 µm, and a nominal lateral resolution of 0.99 µm. Following structural scanning, mice were allowed to rest for 5 minutes to let blood flow equilibrate from brain exposure to room light. The five-minute resting period was observed due to prior reports of red blood cell velocities following optogenetic ChR2 stimulation in the same mouse strain remaining altered for a minute following photostimulation and due to potential pericyte-mediated responses via cytoskeleton reorganization occurring over a minute [6], [30].

Functional scans were acquired over baseline and post-stimulus periods, flanking a period of blue light illumination. The haemodynamic response to optogenetic stimulation in the Thy1-ChR2-EYFP mouse model was previously observed to last about 45 seconds [30], similar to data collected in other optogenetic models of mural cell stimulation where arteries were observed to dilate for approximately 60 and 20 seconds respectively, and capillaries were observed to dilate on the scale of minutes [6], [23]. We thus constrained our volumetric acquisitions to 45 seconds. Each volumetric scan lasted for 42.98 seconds and used the resonant scanner with 5x frame averaging (resulting in a signal-to-noise ratio on the vasculature channel of 6.9±1.6), a nominal lateral resolution of 0.99 µm, a z-step of 2.64 µm, and traversed 250.8 µm of cortical depth. This z-step was chosen because larger z-steps led to discontinuities in the capillary bed segmentation. We imaged the brain in sections from the cortical surface to a depth of 250 µm and from 250 µm to 500 µm of cortical depth. The acquisitions were split into two slabs to maximize the volume coverage without creating discontinuities in the capillary segmentation masks while maintaining a scan duration of under 45 seconds. Stacks were acquired either from the cortical surface down or from the bottom of the stacks toward the cortical surface on different paired acquisitions, so that the post-stimulus delay of image acquisition at different cortical depths was not constant. A 239-um diameter circular photostimulation region was positioned 250 µm beneath the cortical surface. The photostimulation light was raster scanned over this ROI for 5 seconds between imaging scans, with a pixel dwell time of 4 µs for each pixel of the stimulation ROI. Each pixel in the photostimulation ROI was thus excited every 501.55 milliseconds, i.e. at about 2Hz. We used two laser powers for 458-nm photostimulation: 1.1 mW/mm^2 and 4.3 mW/mm^2. The 1.1 mW/mm^2 is just above the threshold for ChR2 photoactivation and is expected to elicit a small degree of neuronal activity, whereas the 4.3 mW/mm^2 photoactivation elicits more neuronal activity while still being below ChR2 saturation level [33], [36]. Low powers were used to activate ChR2-expressing neurons to minimize tissue heating [37]. We also performed control experiments via 552-nm photostimulation (where ChR2 excitation falls to 4% of its peak) at 4.3 mW/mm^2 [38]. Mice rested for approximately 5-7 minutes between scan pairs for the vascular tone to return to its resting state. Photostimulation parameters were presented in randomized order for each mouse.

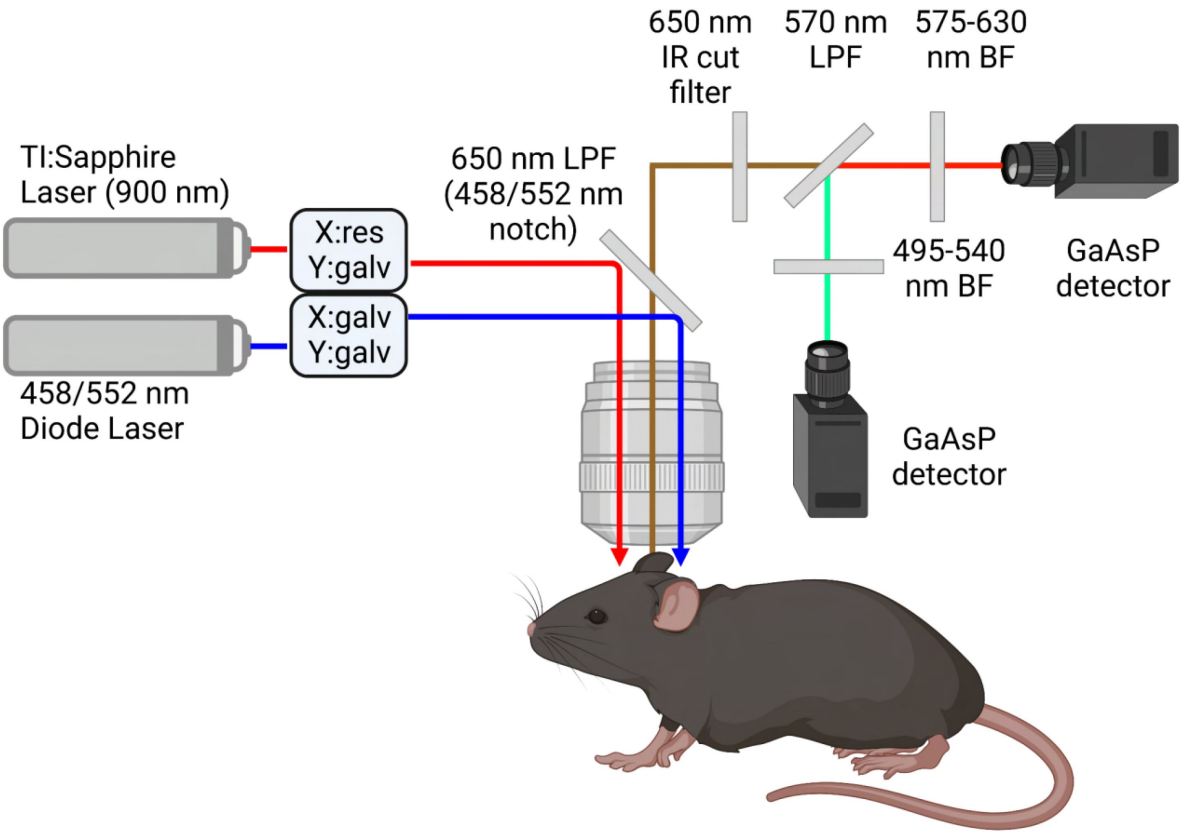

Figure 1

Photostimulation setup:

The excitation and stimulation light pass through a FV30-NDM690 dichroic mirror with two notch filters, at 458 nm and 552 nm, to excite TexasRed, EYFP and ChR2 within the mouse. The emitted light passes through the objective, is reflected off the FV30-NDM690 dichroic mirror, and passes through a 650 nm barrier filter before reaching a 570 nm long pass filter (LPF) separating emitted light from EYFP and TexasRed, which respectively pass through 495-540 nm and 575-630 nm barrier filters to be collected via GaAsP detectors.

3.3 Segmentation and Graph Extraction

Ground truth generation

To generate ground truths, we used ilastik's pixel classification workflow, which relies on random forests, to annotate blood vessels and pyramidal excitatory neurons soma's in 42 volumes from 25 Thy1-ChR2-EYFP mice for training our DL model (24 images from 16 Thy1-ChR2-EYFP mice from other studies were included in the training, validation, and test cohorts to increase our dataset size). Images were semi-automatically segmented in groups of up to 4 each, with a size of 507×507×250 μm each, due to ilastik's inability to handle large amounts of annotations over more than a few volumes. The rater labelled targets (neurons vs. blood vessels), corrected mistakes, and classified the pixels where the output was uncertain (as shown using ilastik's uncertainty guidance feature). During the manual annotation, feature selection was repeatedly optimized using ilastik's suggest feature function (wrapper method), leading to different features being used for the random forest model for each set of images. Small (under 50 pixels) isolated vascular components were removed with connected component analysis in Python using scikit-image and connected-components-3d. Testing data was withheld until the final model was selected based on the models' performance evaluation on the validation data set.

Data preprocessing and augmentation

We used the MONAI python package for data preprocessing, augmentation, model training, and prediction [39]. All images and ground truth segmentation masks were up-sampled to an isotropic voxel size using bilinear and nearest neighbour interpolation. Raw 10-bit image intensities were normalized to range from 0 to 1.0. Each volume had eight 128×128×128 pixel patches randomly cropped out for training. Data augmentation, transformations and parameters are listed in **Supplementary Table 2**. Spatial transformations were selected to expand data variety via cropping, rotations, and mirroring hence exposing the network to images that would be acquired on different positioning of the animal under the microscope. Zooming and deformation transformations were included to expose the network to small changes in the size and morphology of the vasculature. Intensity and Gaussian transformations exposed the network to signal intensity and contrast variations. Dropping pixels was included as the resonant scanner acquisition occasionally yields images with some relatively low signal pixels.

Model Architecture

We trained a state-of-the-art 3D vision transformer (UNETR) model and the U-Net model for baseline comparison, as implemented in PyTorch using the MONAI library [39]. UNETR is a U-Net style architecture with a transformer-based multi-attention head encoder and a CNN decoder. [40], [41]. The encoder takes an input image (or patch from each batch) and breaks it down into a sequence of non-overlapping patches, each of size 16×16×16 pixels, which are weighted differently to account for variation in signal intensities and patterns within an image. The sequence of patches is then passed through a multi-head self-attention and multilayer perceptron encoder to capture self-attention between different pixels of the patch to encode long-range relationships between patches. The encoder is then connected to a CNN decoder with skipped connections to the encoder to map features back onto the original image at multiple spatial scales [40]. The model was trained on 2-channel images (EYFP-expressing neurons and Texas Red-labelled vasculature) as inputs to segment neurons and vasculature. We chose the following parameters for the UNETR architecture: a 12 multi-attention head encoder, 16 convolutional features in the first layer of the encoder, a hidden layer size of 768, a multilayer perceptron size of 3072, and Monte Carlo dropout, where on each run of the model 10% of weights were zeroed [40]–[42].

The U-net model used is based on the original 2D U-net proposed by Ronneberger et al. in 2015 and extended into 3D via 3D convolutional operations and features residual blocks, parametric rectifying linear units, and instance normalization as described by Kerfoot et al. [41], [43]–[47]. The residual blocks were implemented for better gradient flow during the network training. At the same time, the parametric ReLU activation functions were used to improve the ability of the model to adjust its weights during training. Instance normalization was implemented to reduce contrast differences between images fed into the network to improve model robustness. The model was implemented with five layers featuring 16, 32, 64, 128, and 256 channels and dropout. The U-net model was trained using the same data augmentation employed during the UNETR model training.

Model Hyperparameter Optimization, Training, and Prediction

We used a grid search to determine optimal hyperparameters for the UNETR and UNet models within the following parameter space [43], [48]: loss functions (Dice Loss, Dice + Cross Entropy Loss, Dice + Focal Loss, or Tversky Loss), dropout rates (0.1, 0.2, or 0.3), learning rates (5e-3, 1e-3, 5e-4, 1e-4, or 1e-5), and the number of residual units for the Unet model (2 or 3) [49], [50]. We utilized the Adam optimizer [51], and the best model during hyperparameter optimization was selected based on the validation Dice similarity coefficient (DSC) and trained for a maximum of 2400 epochs. The Dice score was the principal evaluation metric, to maximize the overlap between ground truth and prediction masks. Precision and recall were used as secondary metrics to achieve balanced precision and recall where over-segmented results were produced. For early stopping, the epoch with the best performance of the DSC on the validation dataset was selected. The final model that had the best Dice score during hyper-parameter optimization was trained with a Dice + Cross Entropy Loss function, a dropout rate of 0.1, 2 residual units, a learning rate of 1e-5, and a batch size of 1 image with 8 crops per image. Training and optimization were performed on the Narval cluster of Calcul Quebec and the Digital Research Alliance of Canada, with each node using 498 GB of RAM and 4 Nvidia A100 GPUs, each with 40GB HBM2 VRAM.

Ilastik utilized a random forest model from the Vigra library with the default parameters and 100 trees [52], [53]. We initially utilized all default 3D Colour/Intensity/Texture/Edge features during ilastik feature selection and added 2D Colour/Intensity/Texture/Edge features with a sigma of 20.0 pixels. These 2D features were added as a strong, largely planar artifact was observed towards the surface of the images in the neuron channel. We used the wrapper method for feature selection with a set size penalty of 0.10 to determine the optimal features from the starting set. The model was then trained using live updates on the Narval cluster of Calcul Quebec and the Digital Research Alliance of Canada, with each node using 249 GB of RAM and 2 x AMD Rome 7532 CPUs with 64 cores.

For the ilastik model, a subset of 3 training images from 3 mice was used as ilastik's random forest was unable to train a model with more data even on compute nodes with large memory and CPU resources. The model could never complete training within the time limits of the resource allocations. This inability to complete model optimization was expected as ilastik's documentation does not recommend training random forest models with full annotation datasets, and increasing the number of annotations does not necessarily lead to better predictions for the pixel classification workflow [52]. The ilastik random forest model was trained with whole images rather than with patches.

Model Comparison

To compare models, we employed several metrics evaluating the similarity between the ground truth and prediction: the Dice Similarity Coefficient (DSC), Precision, and Recall, as well as surface-based metrics: 95% Hausdorff distance (HD95) and mean surface distance. We specifically focused on mean surface distance and HD95 distance since the centerline extraction used in the downstream analysis was highly sensitive to surface irregularities. The model with the lowest

standard deviation on the mean surface distance was to be selected absent statistically significant differences in the average mean surface distance between different models. Consistency in surface placement was key for extracting good centerlines and graphs from the segmentation masks. The metrics utilized are defined as follows:

$$DSC = \frac{2|X \cap Y|}{|X| + |Y|} \quad (1)$$

$$Precision = \frac{True\ Positives}{True\ Positives + False\ Positives} \quad (2)$$

$$Recall = \frac{True\ Positives}{True\ Positives + False\ Negatives} \quad (3)$$

$$HD95 = Max_{95\%}\{sup_{x \in X} d(x, Y), sup_{y \in Y} d(X, y)\} \quad (4)$$

$$Mean\ Surface\ Distance = \frac{1}{n_X + n_Y}\left(\sum_{p=1}^{n_X} d(p, n_Y) + \sum_{q=1}^{n_Y} d(q, n_X)\right) \quad (5)$$

The DSC measures the overlap between the prediction and ground truth with a value of 1 corresponding to complete overlap. Precision measures the rate of correctly returned predicted values, whereas recall accesses the rate of return of targeted values. Hausdorff 95% distance (HD95) provides the maximum of the 95th percentile of the minimum surface distance between the boundaries of the ground truth and the predicted segmentation mask. The mean surface distance measures the average minimum distance between the surface of the ground truth and the surface of the predicted segmentation mask. Together, the HD95 and mean surface distance assess model performance at the boundaries of the segmentation masks.

Graph extraction of cerebrovascular networks

Graph extraction was performed in Python except for the centerline calculation, which was performed in MatLab (R2021a). Upsampled image acquisitions (0.99 μm isotropic voxel size) were registered with ANTsPy using the rigid registration method with a total sigma of 2 pixels (for smoothing within the registration function) and mean squared error as the similarity metric as input parameters of the *registration* function (**Figure 2A,B**). We selected the first baseline scan from each region of interest that was scanned from the bottom to the top to serve as a reference to which all other images from the same region were aligned. The calculated transforms were used to transform images from the same ROI to the space of the reference image using linear interpolation [54]. We then generated segmentation masks for each aligned image using our trained UNETR model with sliding window inference, and we retained Monte Carlo dropout during prediction to create an ensemble of 20 UNETR models, so as to assess the model uncertainty (**Figure 2D**) [55]. To extract the centerlines, we assumed that no background was present within the vessels, as regions of background within vessels disrupt the centerline extraction algorithm. Background labelled pixels surrounded by blood vessel segmentations were thus filled in using connected component analysis. Disconnected vascular components under 50 pixels were assumed to be noise and removed. Each aligned binary segmentation mask was dilated three times with a footprint defined by scikit-image's disk function with a radius of 1 pixel. Next, we computed the union of all segmentation masks from the same ROI generated from registered images (**Figure 2E**). This common segmentation mask for all time points was eroded to a centerline via a medial axis transformation (*bwskel* function in Matlab (R2021a)). Critically, using the union of all time points minimized the sensitivity of centreline identification to RBC stalls at individual time points. "Hair" segments shorter than 20 micrometres and terminal on one end

were removed to reduce false positive vascular branches [56]. The vascular centerlines were next used to construct vascular graphs (with *sknw*) for each ROI, rendering coordinates of vertices along the vessel's centreline as edges, and branch points as nodes [57].

Based on the vascular graphs, we computed vascular radius estimates at each vertex at each timepoint and then calculated the vertex's distance to the nearest YFP-expressing pyramidal neuron (as measured by the distance transformation at the vertex to the nearest labelled neuron, with the radius of the vessel subtracted off). We employed a two-stage approach to estimate the radius for each point on the centerline. First, using the binary segmentation mask, we calculated the distance from every vessel pixel in the mask to the nearest background pixel. These values were averaged for each vessel to estimate its radius. The radius estimate defined the size of the Gaussian kernel that was convolved with the image to smooth the vessel: smaller vessels were thus convolved with narrower kernels.

In the second stage, the registered raw image was deconvolved with the point spread function of the microscope, as measured via FluoSpheres carboxylate-modified Microspheres (Cat# F8803, Thermo Fisher Scientific Inc, Waltham MA), using Richardson-Lucy deconvolution. To low pass filter the centreline in advance of computing the tangent vector at each vertex, the coordinates of the vertices along the centerline were smoothed using a Gaussian with a sigma of 3. Next, the tangent vector to the centerline was specified by calculating the gradient of the centerline path. Given this local tangent to the vessel's direction of travel at a given vertex, we extracted image intensities in the orthogonal plane from the deconvolved raw registered image. A 2D Gaussian kernel with sigma equal to 80% of the estimated vessel-wise radius was used to low-pass filter the extracted orthogonal plane image and find the local signal intensity maximum searching, in 2D, from the center of the image to the radius of 10 pixels from the center. The orthogonal plane image was sampled every 10 degrees (as finer radial sampling did not improve the estimation) along radial lines emanating from the local signal intensity maximum closest to the center of the image and 5x bicubic upsampled to extract thirty-six 1D signal intensity profiles at that vertex, as shown in **Figure 2H**. These line profiles were then convolved with a 1D Gaussian kernel with a sigma of 80% of the estimated radius of that vessel, and the gradient of each profile was calculated as shown in **Figure 2I**, J. The vessel boundary was then placed at the local minimum of the gradient of each profile. The mean and standard deviation of the boundary distances for the thirty-six 1D line profiles were calculated, and boundary points greater than 2 standard deviations away from the mean were excluded (**Figure 2K**). This radius estimation procedure was repeated for all vertices of all vessels.

In the last step, we computed the distance from each image voxel to the nearest YFP-expressing pyramidal neuron by computing the distance from every image pixel not belonging to the neuron mask to the closest YFP-expressing neuron's soma boundary (based on the neuron's binary segmentation mask). At the vessel vertices, these distances were adjusted by subtracting the vessel's radius. We thereby captured the distance from the vessel surface to the closest YFP-expressing neuron.

Boundary detection validation

To assess the uncertainty in the radius estimates at each vertex, we simulated changes to the vascular diameter by "resizing" the extracted orthogonal plane image and adding Gaussian noise to it. These steps were undertaken to validate the ability of the boundary detection method to estimate diameter changes and evaluate the robustness of the estimates to increased amounts of noise. For the diameter change estimation, images were resampled from the orthogonal plane by a random factor, uniformly distributed in the range of 0.5x to 2x. Then, the aforementioned boundary detection methods were used to estimate vertex-wise calibre changes. The end goal of the assessment was to see how close the boundary detection method-based radius change matched the prescribed diameter change. In the second task, we added Gaussian noise with a sigma

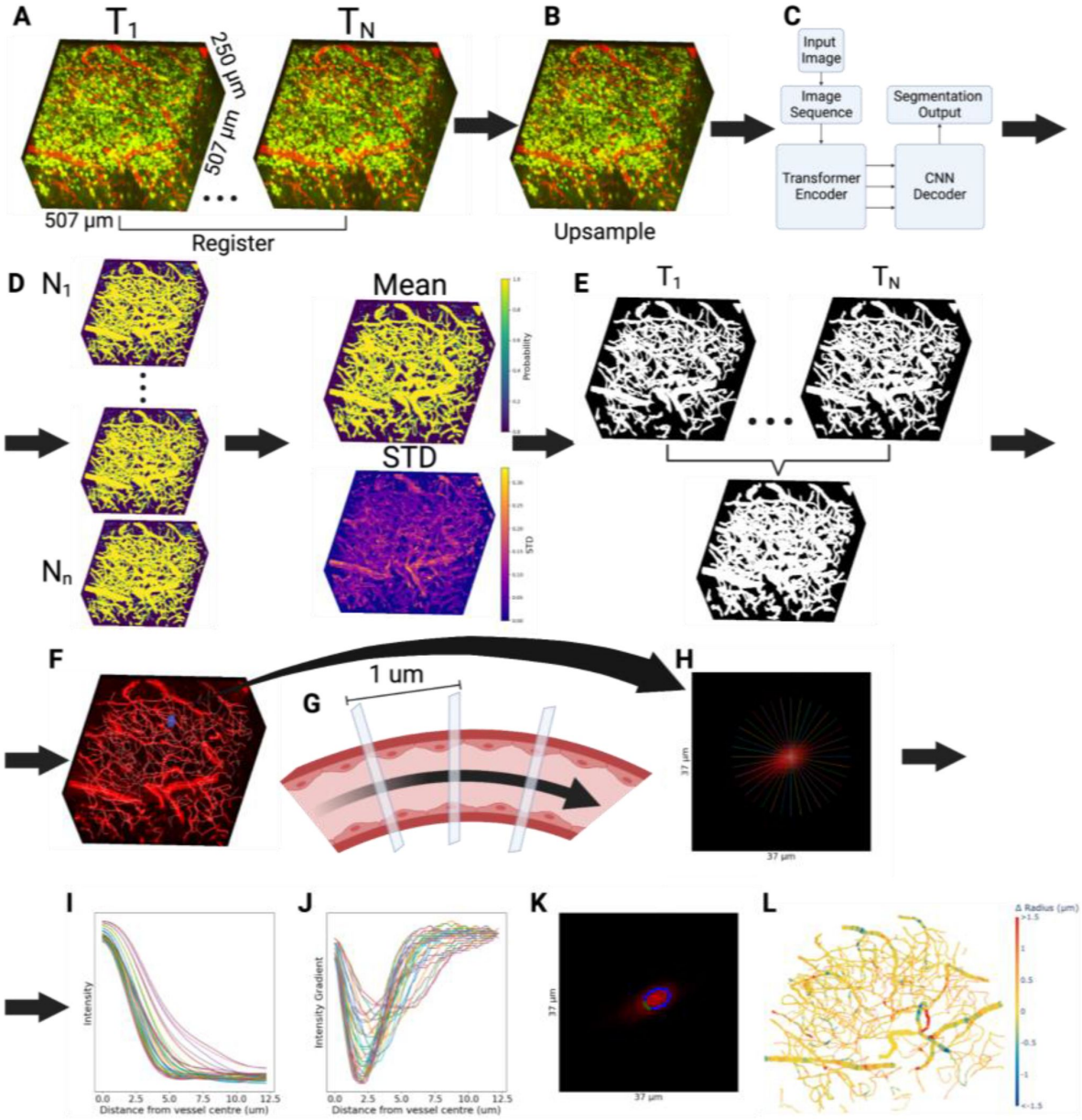

Figure 2.

Computational analysis pipeline:

A. The stacks of 2PFM slices were registered using ANTS rigid registration and aligned to the reference time point. **B.** Images were upsampled using bicubic interpolation to an isotropic resolution of 0.99×0.99×0.99 µm. **C.** An ensemble of UNETR deep learning models with dropout generated segmentation masks at each time point, producing probability maps. **D.** The mean and standard deviation of the probability of each pixel being vasculature were computed and used to create binary vascular segmentation masks. **E.** The union over the vascular segmentation masks for all time points was computed, and background pixel clusters within vessel masks were removed. **F.** The vascular segmentation mask was thinned down to centerlines and rendered as a graph, where edges were vessel segments connecting branch points (nodes). This skeleton was overlaid on the vasculature channel from which the neuron channel was subtracted. **G.** The plane orthogonal to the tangent to the vessel's travel direction was computed every micrometre along the centerline. **H**,**I.** 1D signal intensity profiles at each centerline vertex were computed in the orthogonal plane every 10°. **J.** The boundary for each profile was placed at the minimum of the signal gradient for that signal intensity profile. **K.** The raw intensity image with the detected boundary points, where outlier boundary points (in green) were defined as points over 2 standard deviations from the mean and excluded. **L.** Visualization of the changes in vertex-wise radii on a sample vascular network.

randomly chosen from a uniform distribution ranging from 0 to 500 SU to the orthogonal plane image. The noise was added to the image after deconvolution with the PSF and the extraction of the orthogonal plane but before Gaussian smoothing. We then reported on the percent change in the radius as a result of resizing or adding noise in relation to the baseline radius.

3.4 Vascular Network Analysis

Leveraging the graph representation of the vasculature in our pipeline, we next used graph theory to better understand the networks' behaviour upon neuronal activation. We looked at morphometrics including vascular segment count density, vascular length density, and mean vessel length for comparison with other work. To demonstrate the benefits of extracting a graphical representation of the vasculature in situ, we looked at graph theory metrics including the assortativity of vascular radius changes and changes to the global efficiency of the capillary (below 5 μm in radius) network following optogenetic stimulation. The assortativity measures the tendency for one vessel to dilate or constrict by a similar amount as its neighbours. The assortativity (q) of radius changes in response to stimulation is defined as the Pearson correlation coefficient of these changes on connected vessels:

Assortativity

$$q = \frac{\sum_{xy} \; xy(e_{xy} - a_x b_y)}{\sigma_a \sigma_b} \tag{6}$$

where e_{xy} represents the fraction of vessels (edges) in the network that join together nodes with values x and y (i.e. radius changes with values x and y); a_x and b_y are the percentages of edges connecting nodes with values x and y, and $\boldsymbol{\sigma}_a$ and $\boldsymbol{\sigma}_b$ are the standard deviations of a_x and b_y [58]. The efficiency, in turn, captures how easily the graph can be traversed. For vascular graphs, efficiency can be conceptualized as the average of the inverse of the total resistive distance of the shortest paths of all combinations of vascular junctions, with the hydraulic resistivity serving as the distance between them. The resistivity (equation 7) is summed along the shortest paths, and the inverse of this sum is then averaged across all shortest paths to compute the efficiency (equation 8). Finally, pPhotostimulation-induced change in the efficiency, from its baseline level, is reported.

Resistivity

$$\rho = \frac{8\mu L}{\pi R^4} \tag{7}$$

Efficiency

$$E = \frac{1}{N(N-1)} \sum_{i \neq j \in V} \frac{1}{\rho_{ij}} \tag{8}$$

In computing resistivity, we assumed a fluidic viscosity (μ) of 4 cP which is within the physiological range [59]; L was the length of the capillary; and R was the radius of the capillary. Vessels greater than 10 μm in diameter were excluded from the efficiency calculation as we wanted to examine blood flow through the capillary nexus between arteries and veins where blood flow may be reversible [60]. The sum of the resistivities along the least resistive path specified ρ_{ij} in the efficiency calculation: this sum quantifies how hard it is for blood to move through the said microvascular bed. N refers to the number of nodes in the network. The efficiency was calculated as the average of the inverse of the least resistive paths between all pairs of nodes. The efficiency increases with increasing radius on the shortest paths through the network.

3.5 Statistical models

To statistically compare deep learning model performance, we used the Wilcoxon signed-rank test as implemented in *scipy* (1.9.3) [61]. Statistics for vascular radius and network metrics were performed in R (4.3.1) using restricted maximum likelihood mixed effects models as implemented in lme4 (1.134) [62], with post hoc comparisons done using *emmeans* (1.8.8) [63]. We ran the

following linear mixed effects model, separately on dilating and constricting vessels that exhibited radius changes above two standard deviations of the vessel's baseline radius, to examine the effects of photostimulation power on microvascular radius changes in responding vessels:

$$\Delta\text{Radius} \sim \text{Stimulation} + (1|\text{Vessel})$$

Due to the difference in their vessel wall ultrastructure, larger microvessels (above 5 μm in radius) were examined separately from capillaries (radius < 5 μm).

For graph metrics, we included nesting of the field of view within each subject as a random effect so as to account for differences in vascular network architecture within an individual. The linear mixed effects models for the graph metrics used were as follows:

$$\text{Assortativity} \sim \text{Stimulation} + (1|\text{Subject/Field of View})$$

$$\Delta\ \text{Efficiency} \sim \text{Stimulation} + (1|\text{Subject/Field of View})$$

In Tables and text, all values have been quoted as mean ± standard deviation, unless otherwise specified.

4 Results

Application of our computational pipeline resulted in robust segmentation of the vasculature and neurons from 4D in situ 2PFM images and rendering of the microvasculature as a graph. The vessel-wise and vertex-wise calibres were tracked across stimulation conditions and related to the cortical depth and the distance to the closest YFP-expressing neuron, mapping the network-level vascular responses to ChR2 activation and revealing the coordination of the microvascular responses following neuronal activation.

4.1 Segmentation model results and comparisons

We compared an ensemble of UNETR models, an ensemble of U-Net models, and an ilastik random forest model on a test dataset of 9 images (507×507×250 μm each) from 6 mice. Examples of segmentation masks produced by each of the models are shown in **Figure 4**. When evaluating model performance, we paid close attention to the smoothness of the surface of the segmentation masks due to the sensitivity of the centerline extraction algorithms to irregularities in the surface of the masks: smoother vascular segmentation masks resulted in fewer falsely identified vessel branches. Ilastik tended to over-segment vessels, i.e. the model returned numerous false positives, having a high recall (0.89±0.19) but low precision (0.37±0.33) (**Figure 3**, **Supplemental Table 3**). When comparing the UNETR and U-Net models, we focused on the surface-based mean surface distance and HD95 distance metrics. Since we observed no significant differences in these metrics between the two models, we selected the UNETR model as our final model because it produced more consistent segmentations on visual inspection and showed significantly better performance than ilastik on HD95 for both vessel and neuron segmentation ($p < 0.05$).

4.2 Vessel extraction improvements via image registration

Rigid registration across all time points from the same field of view improved the ability to trace vascular paths from in situ 2PFM data. Firstly, registration decreased the mean squared error (MSE) between acquisitions from 1306±747 to 0.008±0.003 Signal Units. The number of images acquired per field of view ranged from a total of 2 to 10 depending on how many repeats were

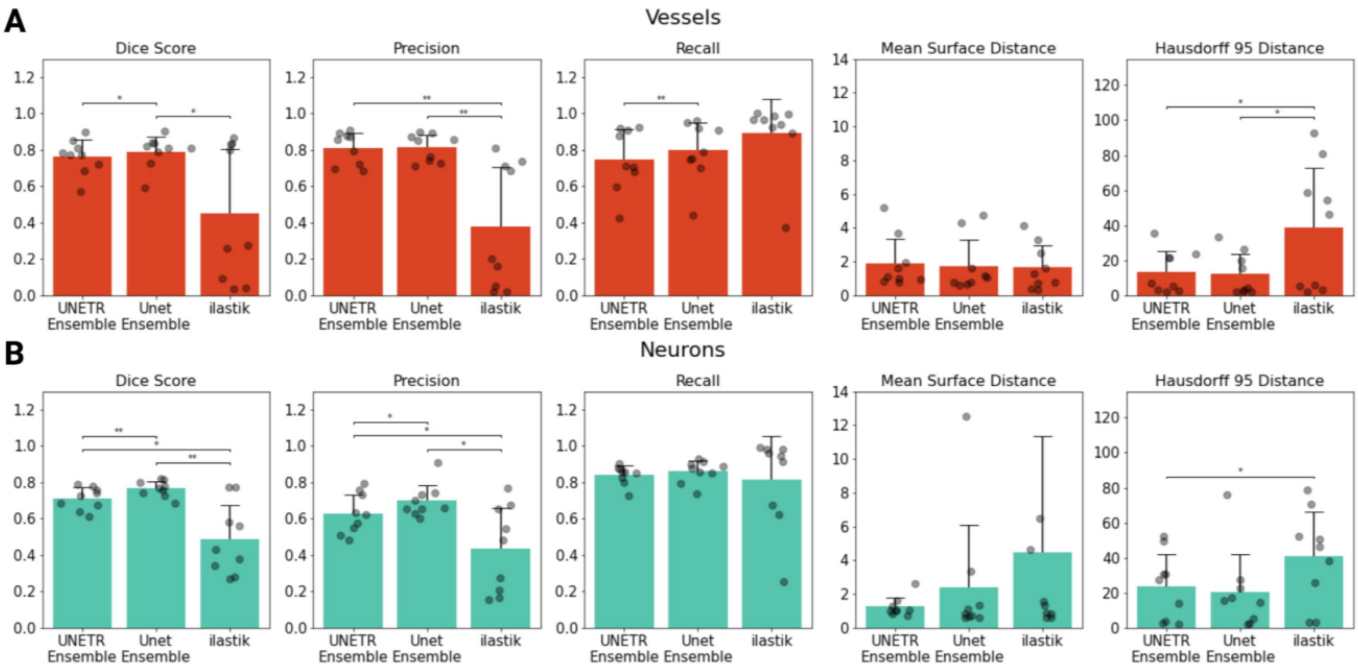

Figure 3.

Model performance metrics:

The Dice, precision, recall, mean surface distance, and HD95 distance for the vascular (**A**) and neuron (**B**) channels. Each model was evaluated on the same test dataset composed of 9 images (250×507×507 µm each) from 6 mice. A Wilcoxon signed-rank test was used to compare the model's performance on each performance metric for images from the test dataset. * $p < 0.05$, ** $p < 0.005$, and *** $p < 0.0005$. p-values were not adjusted.

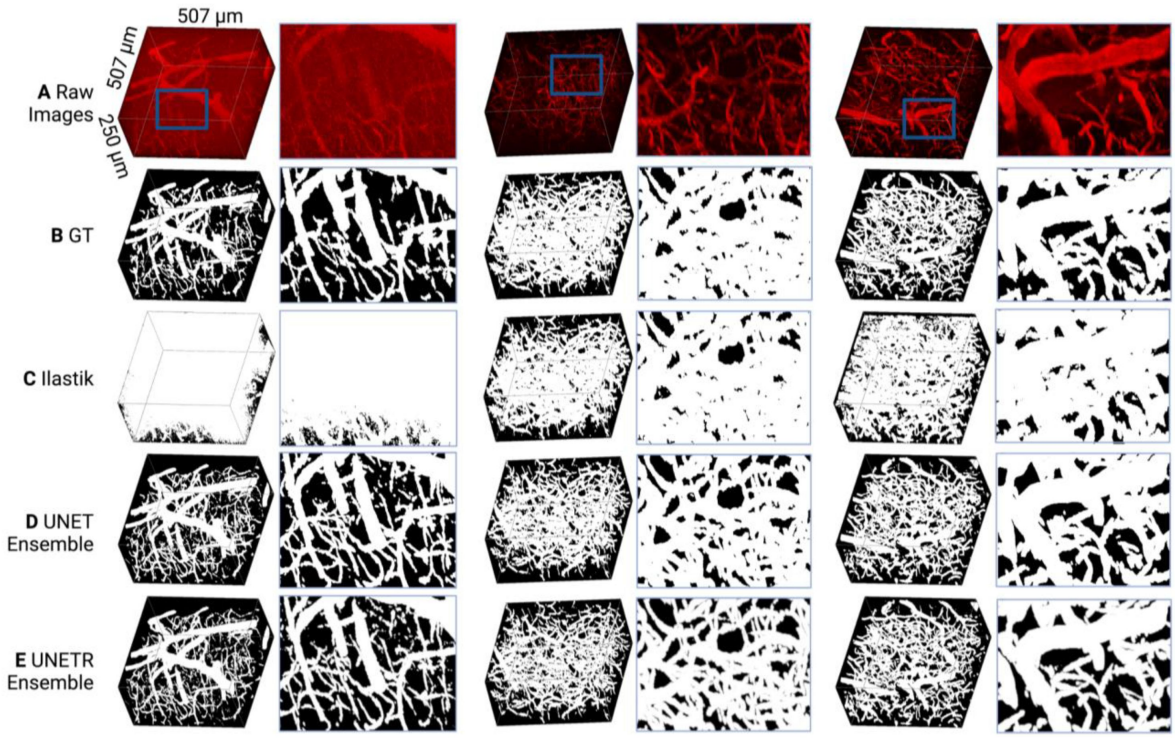

Figure 4.

Visual model comparison:

A. Raw images of the vascular channel with the neuron channel subtracted to facilitate vessel visualization. The first and last stacks in each row span from the cortical surface to 250 µm below the surface, while the middle stack spans from 250 µm below the surface to 500 µm below the surface. All images were from the test dataset, which was unseen during model training. **B.** Ground truth segmentation masks for the vasculature were generated by a rater who utilized ilastik-assisted manual segmentation. **C.** Ilastik predictions generated via a random forest model. **D.** Binary segmentation masks generated by an ensemble of 3D UNet Models. **E.** Binary segmentation masks generated by an ensemble of 3D UNETR models.

able to be acquired. Registration enabled the computation of the union of segmentation masks from all time points. This increased the number of vessel segments identified in each field of view from 241±174 based on a single time point to 412±281 vessel segments per field of view (507×507×250 μm, n=107 fields of view). Taking the union of segmentation masks of an image stack across all time points substantially decreased the incidence of gaps in capillaries, likely arising due to "transient RBC plugs." The pipeline's ability to reconstruct the cortical vascular network was thus significantly improved by registering data obtained at different time points.

4.3 Validation of pipeline sensitivity to geometric changes

To evaluate the ability of our computational pipeline to detect vessel caliber changes of various magnitudes, we simulated a range of vascular caliber changes and injected various levels of Gaussian noise. Across >100,000 simulations, the fit of the estimated radius following rescaling against the simulated radius had an R^2 value of 0.68. **Figure 5B** presents a heatmap of the estimated radius post-scaling vs. simulated radius, across different vertices of vessel centerlines, highlighting the ability of our pipeline to estimate vascular radii accurately. The addition of Gaussian noise revealed the robustness of the pipeline: radius estimates remained stable with increasing noise levels, until the addition of noise with a standard deviation of over 200 SU (with the intensity of the images ranging from 0 to 1023 SU).

4.4 Vascular morphology and heterogeneity within and among vessels

Segmentation coupled with graph extraction enabled a detailed characterization of the microvascular network properties. The morphological properties of extracted networks are listed in **Table 1**, with the probability densities of the vessel length, baseline vessel radius, mean vessel segment depth, and vessel branch point depth shown in **Supplementary Figure 3**. On the extracted graphs, the vascular radius and distance to labelled neurons were sampled every 1-1.73 μm, enabling detailed analysis of the relationship between the vessel radius change and the proximity to the YFP-expressing neurons. The radius was tracked across different time points, permitting the analysis of the stimulation-induced change in the vascular caliber. To highlight the ability of the pipeline to detect vessels that significantly change their radius after stimulation, **Figure 6A** shows the standard deviation of the average radii on each vessel segment during baseline frames for three mice. There was a large difference in this standard deviation across various blood vessels, showcasing the model's ability to reveal baseline variations within each subject. We examined the average change in the vascular radius of each vessel segment after vs. before photostimulation (**Figure 6B**), with even finer spatial patterns detected by analyzing the vertex-wise radius changes (**Figure 6C**). The vascular diameter changes were related to the distance from the vessel's surface to the closest pyramidal neuron at each vertex of the centerline (**Figure 6D**). The vertex-wise radii estimation allowed the assessment of the variations in radii changes within individual blood vessels (**Figure 7**). Notably, capillary radius varied along the vessel length across the baseline frames, by 24 ± 28% of the mean resting radius. Consequently, point measurements in vessel calibers - that are widely reported in the literature - do not permit accurate estimation of the microvessel volume changes. Together, the within- and across-vessel radii estimations illustrate the pipeline's ability to capture spatial variations in the vascular reactivity and relate it to other morphological features (e.g., the distance to the closest activated neuron).

4.5 Vascular reactivity to optogenetic stimulation

The ability of the pipeline to reveal novel spatial relationships between the vascular network reactivity and neuronal activation was demonstrated by examining the relationship between photostimulation-induced microvascular radii responses and 1) the closest YFP-labelled pyramidal neurons within 80μm, and 2) the cortical depth, at the vertex-wise level and across different

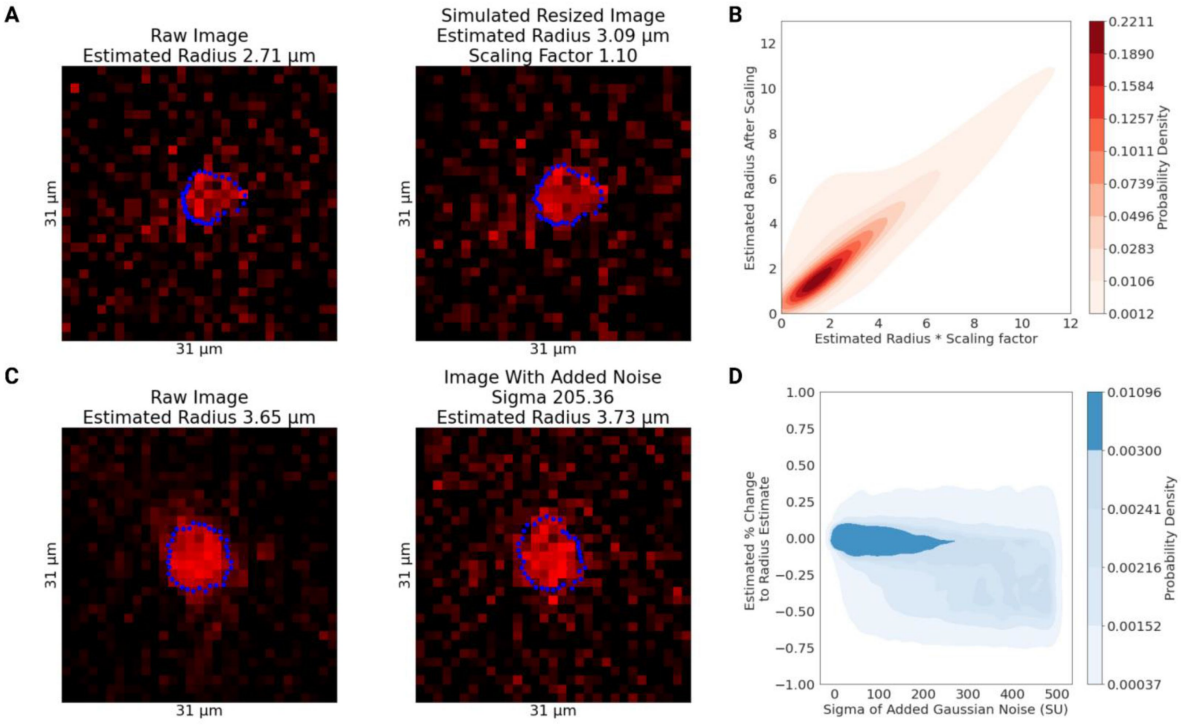

Figure 5.

Estimation of simulated radii changes:

A. An image in the plane orthogonal to the local tangent to a capillary with the detected boundary (in blue) and with the estimated radius of 2.28 µm. On the right, this image was resized (upsampling, via bicubic interpolation, by 1.10 times) to simulate dilation. **B.** The plot shows correspondence between the estimated radius following scaling and the simulated level of scaling. **C.** An image in the plane orthogonal to the local tangent of a capillary with the detected boundary (in blue) and with the estimated radius of 3.65 µm. On the right, Gaussian noise with a sigma of 205.36 SU was added to the image. **D.** The estimated % change in the vessel's radius after the addition of varying levels of Gaussian noise, demonstrating the robustness of the radius estimated to noise.

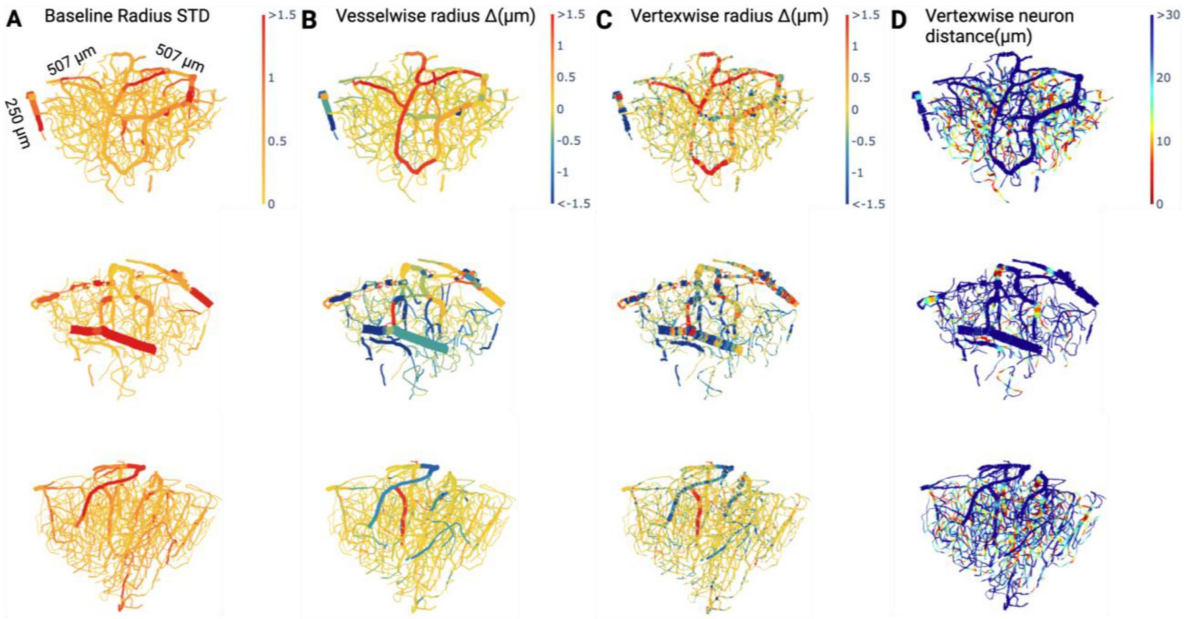

Figure 6.

Vascular graph examples:

A. Baseline variability in vessel diameter estimated by the standard deviation of each vessel's mean radius across baseline time frames. **B.** Mean change in the vessel radius induced by optogenetic stimulation. **C.** Mean change in the vertexwise radius, allowing the visualization of heterogeneity of radius changes within each vessel. **D.** Distance from each vertex to the closest pyramidal neuron. Each row corresponds to the vascular graph of a different mouse.

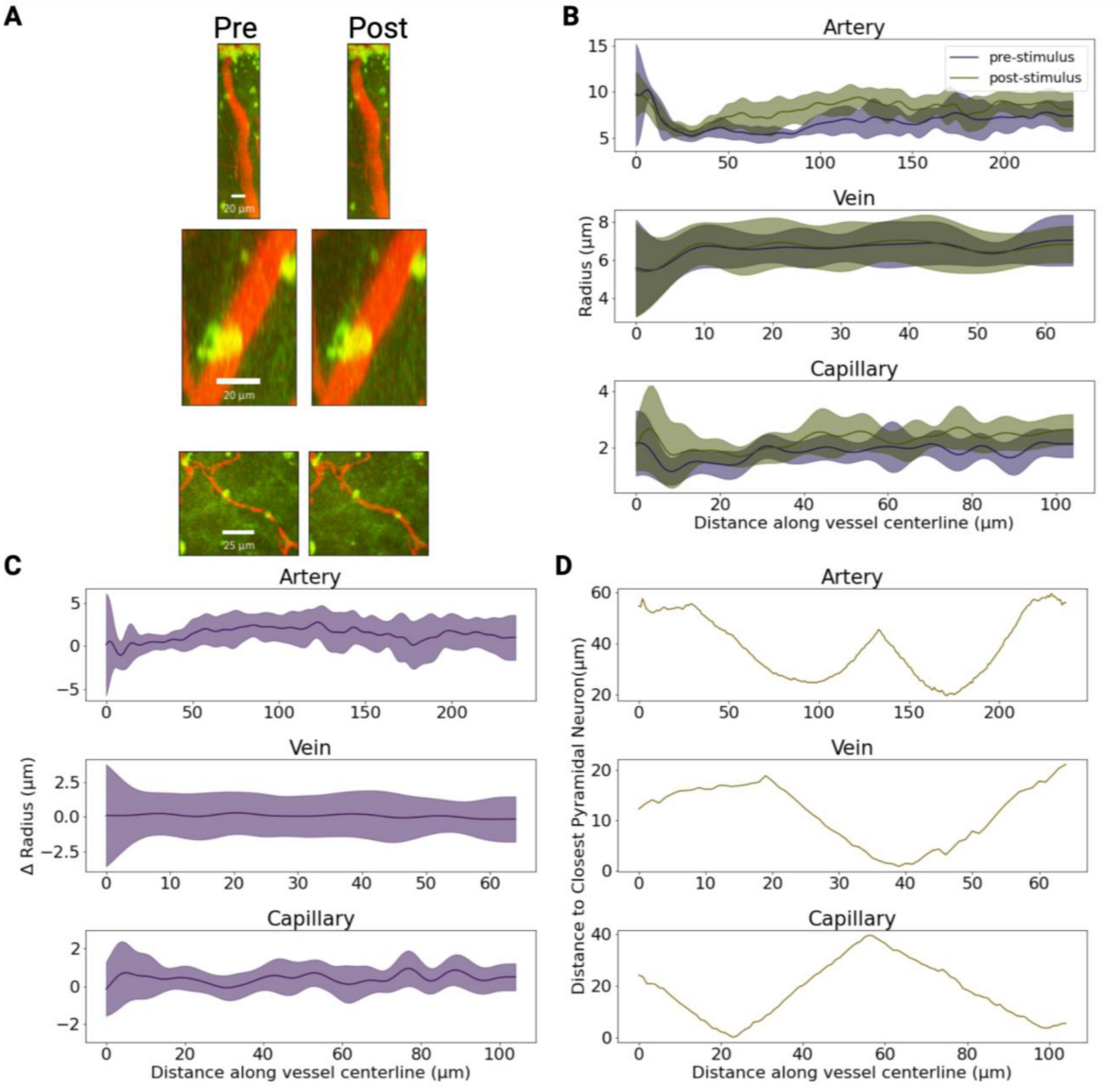

Figure 7.

Vertex-wise radii along vessel lengths of a sample artery, capillary and venule at baseline vs. post-stimulation:

A. MIP of an artery, vein, and capillary segments before (left) and after (right) optogenetic stimulation with 458nm light at 1.1 mW/mm^2. The artery and capillary dilated by 1.33±0.86 µm and 0.42±0.39 µm, respectively (for both p<1e-4, Mann-Whitney U test), whereas there was no significant change in the venular caliber upon photostimulation (p=0.22, Mann-Whitney U test). **B.** Estimates of the vertex-wise radius obtained along each of the three vessels' centrelines, before and after stimulation. **C.** Vertex-wise radii changes in response to optogenetic stimulation. **D.** The vertex-wise distance from the vascular surface to the closest YFP-expressing neuron.

Metric	Mean ± SD	N = 17 Mice (9M/8F)
Number of Individual Vessels per Volume	368 ± 239	32 FOVs
Vessel Density	5705 ± 3705 mm^{-3}	32 FOVs
Number of Vascular Junctions per Volume	207 ± 154	32 FOVs
Vascular Junction Density	3215 ± 2385 mm^{-3}	32 FOVs
Number of Terminal Vessels per Volume	128 ± 52	32 FOVs
Individual Vessel Length	70.7 ± 61.1 µm	12555 vessel segments
Cumulative Vessel Length Density	0.40 ± 0.22 m/mm^3	32 FOVs
Baseline Vessel Radius	2.19 ± 1.66 µm Range: 0.66-15.88µm	12555 vessel segments
Baseline Intra-Vessel Radius Standard Deviation	0.53 ± 0.47 µm	12555 vessel segments
Baseline Vascular Volume Density	0.010 ± 0.007 mm^3/mm^3	32 FOVs
Number of Pyramidal Neurons per Volume	313 ± 202 Neuronal Somas	32 FOVs
Pyramidal Neuron Density	4872 ± 3145 Neuronal Somas/mm^3	32 FOVs

Table 1

S1FL Vascular Network Morphological Properties

photostimulations (**Figure 8**). Vessels were coarsely segregated into small (average radius < 5 μm) and large (average radius > 5 μm) vessels, as we expected them to respond differently due to their differential wall-associated cell composition. Only vessels that significantly responded following optogenetic stimulation were analyzed: a vessel was deemed a responder if its radius changed by more than twice the baseline standard deviation in the vessel's radius. The morphometric properties of the responders, under different stimulation conditions, are listed in **Table 2**. The average magnitude of the capillary radius change was 1.04 ± 1.11 μm. The variability in the radius change within the vessel was higher in the dilating vessels, 0.77 ± 0.61 μm, then in the constricting vessels, 0.69 ± 0.49 μm, for 458-nm, *4.3* $\frac{mW}{mm^2}$ photostimulation (p<1e-4) (with no statistically significant changes detected for 458-nm, *1.1* $\frac{mW}{mm^2}$ photostimulation, and 552-nm, *4.3* $\frac{mW}{mm^2}$ photostimulations). Excluding vessels that did not change their radius by over twice the baseline standard deviation removed almost all large vessels from this analysis (Notwithstanding, **Supplemental Figure 3** depicts unfiltered large vessel constrictions and dilations.) We ran mixed effects models (at the vessel level) separately on constricting and dilating vessels to investigate the effect of optogenetic stimulation power on the vessel radius changes. Each of the models was run separately on small and large vessels.

4.5.1 Vessels further away from activated neurons constrict while those closer to the activated neurons dilate

We examined the relationship between vascular radius changes and the distance to the closest labelled pyramidal neuron, as microvascular response is thought to result from neuronal activation-elicited generation of vasoactive molecules that diffuse to the neighbouring vessels. For the control condition (552nm, *4.3* $\frac{mW}{mm^2}$ photostimulation), 2.9% of small capillaries dilated while 1.0% of small capillaries constricted; in larger vessels, barely any responded (0.4% dilated). For this control condition, there was no significant difference in the distance from constrictors or dilators to the closest pyramidal neuron. For the 458 nm photostimulation, capillary constrictors were on average farther away than were dilators from the activated pyramidal neuron: dilations occurred 16.8 ± 13.5 μm away from activated neurons while constrictions occurred 22.7 ± 16.3 μm for *1.1* $\frac{mW}{mm^2}$ photostimulation (p=1.5e-3) whereas the *4.3* $\frac{mW}{mm^2}$ photostimulation had dilations occur 16.1 ± 14.3 μm away and 21.9 ± 14.6 μm for constrictors (p<1e-4). There was no significant shift between the distance from vessels to neurons for the 1.1 $\frac{mW}{mm^2}$ and 4.3 $\frac{mW}{mm^2}$ stimulations with 458 nm light.. Dilations in capillaries following 458 nm photostimulation were larger than those following the 552 nm control photostimulation: 0.90 ± 0.93 μm dilatations occurred with 1.1 $\frac{mW}{mm^2}$ and 0.90 ± 0.78 μm with 4.3 $\frac{mW}{mm^2}$ at 458 nm; vs. 0.58 ± 0.92 μm with 4.3 $\frac{mW}{mm^2}$ at 552 nm (p<1e-4). For constrictions, 458 nm photostimulations led to -1.39 ± 1.51 μm radius changes with 1.1 $\frac{mW}{mm^2}$ and -1.20 ± 1.13 μm radius changes with 4.3 $\frac{mW}{mm^2}$ (p=4.4e-3); whereas 552 nm photostimulation induced -0.37 ± 0.30 μm radius changes with 4.3 $\frac{mW}{mm^2}$ of power, which was smaller than the 458-nm induced responses (p=0.02).

4.5.2 Vascular radius changes at increasing cortical depths

Vascular responses were next segregated by the cortical depth of the vessel (i.e. the average vessel distance from the cortical surface) [64]. Dilators tended to be located closer to the cortical surface across all stimulation conditions. Constricting vessels were located at an average 58 ± 187

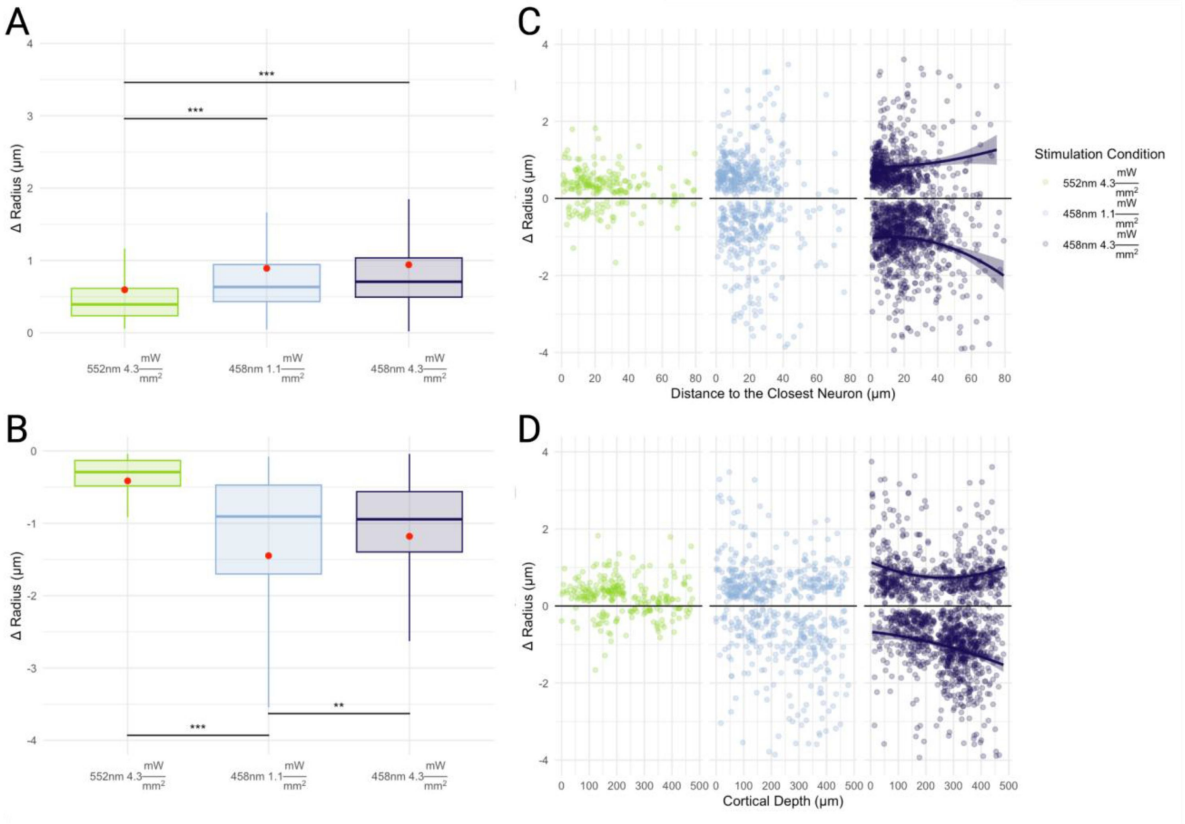

Figure 8.

Optogenetic activation-induced changes in vessel-wise microvascular radii:

Capillary responses included both dilatations, shown in **A.** and constrictions, shown in **B.**, with changes in the magnitude of the capillary response with increased photostimulation power. * $p < 0.05$, ** $p < 0.005$, and *** $p < 0.0005$. p-values were not adjusted. **C.** Changes to capillary radii are displayed in relation to the closest pyramidal neurons. The proportion of vessels constricting increased with the higher intensity of blue light stimulation, and constrictions tended to occur further away from pyramidal neurons than did dilations. **D.** Mean cortical depth of responding capillaries showed a tendency for dilators to be closer to the surface and for constrictors to be deeper in the tissue.

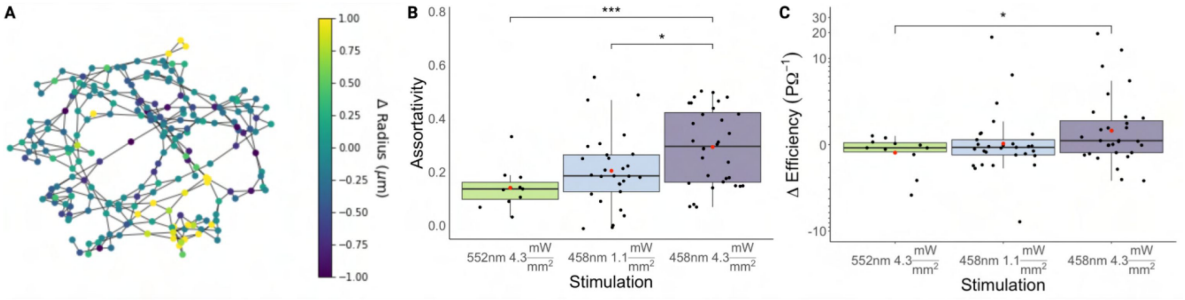

Figure 9.

Microvascular Network Coordination Following Optogenetic Stimulation:

A. Graph representation of a vascular network of 425 vascular segments from a single image stack. Vessel segments are depicted as nodes of the graph; vascular segments that are joined at junctions are connected by edges. Nodes are coloured by the change in the mean vessel-wise radius following photostimulation with 458 nm light at 4.3 mW/mm^2. **B.** Assortativity of photostimulation-induced changes in mean capillary radius increased with increasing photostimulation power. **C.** Photostimulation-induced changes in the efficiency of the capillary network. The capillary network efficiency changed by a median -0.16 PΩ^{-1} (IQR: -0.39 to 0.10 PΩ^{-1}) in response to green light; -0.14 PΩ^{-1} (IQR: -0.55 to 0.27 PΩ^{-1}) in response to lower intensity bluelight; and 0.22 PΩ^{-1} (IQR = -0.43;1.47 PΩ^{-1}) in response to higher intensity blue light.. There was a significant increase ($p = 0.03$) in the capillary network efficiency post 458-nm light at 4.3 mW/mm^2, when compared to that following the control green illumination. The measurements came from 72 paired acquisitions of 32 image stacks acquired in 17 mice (9M/8F). * $p < 0.05$, ** $p < 0.005$, and *** $p < 0.0005$. p-values were not adjusted.

Stimulation Condition	Total number of vessel estimates	Average Minimum distance to the closest neuron (µm)	Number of Dilators	Minimum distance from dilators to the closest neuron(µm)	Average vessel depth of dilators (µm)	Diameter change (µm)	Number of constrictors	Minimum distance from constrictors to the closest neuron(µm)	Average vessel depth of constrictors (µm)	Diameter change (µm)
All Vessels			**Dilators**				**Constrictors**			
Capillaires										
552 nm 4.3 $\frac{mW}{mm^2}$	5036	21.2 ± 16.2	144 (2.9%)	25.5 ± 19.0	186 ± 114	0.58 ± 0.92	49 (1.0%)	26.5 ± 19.5	247 ± 122	-0.37 ± 0.30
458 nm 1.1 $\frac{mW}{mm^2}$	10136	18.7 ± 14.5	317 (3.1%)	16.8 ± 13.5	196 ±138	0.90 ± 0.93	255 (2.5%)	22.7 ± 16.3	254 ± 126	-1.39 ± 1.51
458 nm 4.3 $\frac{mW}{mm^2}$	12537	20.6 ± 15.4	575 (4.6%)	16.1 ± 14.3	237 ± 146	0.90 ± 0.77	974 (7.7%)	21.9 ± 14.6	274 ± 103	-1.19 ± 1.13
Large Vessels										
552 nm 4.3 $\frac{mW}{mm^2}$	225	43.1 ± 19.5	1(0.4%)	75.4	82	13.98	0 (0%)	NA	NA	NA
458 nm 1.1 $\frac{mW}{mm^2}$	545	38.4 ±19.5	1 (0.2%)	26.1	402	1.97	1 (0.2%)	19.0	179	-3.65
458 nm 4.3 $\frac{mW}{mm^2}$	569	38.4 ± 20.1	2 (0.35%)	53.1 ± 6.3	84 ± 34	2.47 ± 2.93	6 (1.1%)	43.1 ± 16.3	290 ± 125	-6.07 ± 2.45

Table 2

Details of responder vessels

μm deeper than dilators for 458-nm stimulation at 1.1 $\frac{mW}{mm^2}$ (p=0.02), and 37 ± 179 μm deeper for 458-nm photostimulation at 4.3 $\frac{mW}{mm^2}$ (p<1e-4) (with no change in the mean depth of either constricting or dilating vessels with changes in the photostimulation power).

4.5.3 Vascular Network Coordination Following Optogenetic Stimulation

We examined the coordination of changes in the microvascular network as a whole via assortativity of radius changes and network efficiency changes. The vessel responses were observed to be assortative, i.e., capillaries mirrored the responses in their neighbours. The increases in stimulation power were accompanied by increases in the assortativity of capillary responses: increasing stimulation level resulted in heightened coordination between adjacent capillaries.

The efficiency increased only at the strongest blue photostimulation, i.e., only at this level of stimulation did the resistivity along the average of all of the shortest paths between junctions in the vascular network decrease, resulting in attenuated resistance to flow through the network. The distribution of changes to the efficiency were highly skewed (with a coefficient of skewness of -1.06 for green illumination, 2.92 for lower intensity blue photostimulation, and 4.87 for higher intensity blue photostimulation). The median increase in the efficiency induced by the higher intensity blue photostimulation, of 4% (IQR: -8% to 38%), was significantly higher than the median -6% (IQR=-9% to 4%) efficiency change following the control green illumination

5 Discussion

Recent studies have demonstrated temporal propagation and coordination in cerebrovascular responses to neuronal activation, whereby arteries dilated after capillary exposure to increased potassium ion concentration [65]; opposing geometric changes have been reported by some studies in capillaries connected by intercapillary tunnelling nanotubes [24]. However, how the effects of these and other mechanisms influence in situ reactivity of the 3D brain capillary network remains unknown. Here, we developed a pipeline for extracting graphs of brain microvascular networks from in situ 2PFM and examine coordination within and across capillaries. Capillary networks and their geometrical changes were imaged via 2PFM during periods of baseline alternated with photostimulation of ChR2 in pyramidal neurons of transgenic mice, and the microvascular mesh was evaluated every 1-1.73 μm. The vascular morphology was then analyzed vertex- and vessel-wise across the entire network. All vessels exhibited significant heterogeneity in caliber changes along their length. Neuronal activation induced both dilations and constrictions of vessels and the incidence of constrictions increased with increasing cortical depth. As the stimulation power increased, the tendency for vessels to change their radius by an amount similar to their neighbours increased. Only the highest photostimulation intensity elicited an increase in the network efficiency. Our findings reveal an intricate level of coordination among brain microvessels and provide a computational analysis platform for interrogating a host of hypotheses on cerebral microvascular reactivity.

Vascular Segmentation and Network Extraction

Intensity thresholding-based image processing pipelines have been used to examine vascular networks and quantify vascular morphology, but they have not gained widespread use due to difficulties in adapting them to highly heterogeneous levels of noise across samples [66]–[69]. Deep learning-based methods for analyzing vascular morphology from 3D microscopy images have become prevalent as they provide robust segmentation results over a wide range of signal-to-noise ratios. Recent work has demonstrated steady improvements of segmentation models' performance with respect to similarity-based metrics (i.e., Dice scores) [70]–[75];

though surface-based metrics may be better predictors of how amenable segmentation outputs will be to subsequent morphological analysis of the microvascular network. Our final UNETR model was selected based on a combination of performance metrics including mean surface distance, Hausdorf 95% distance, and rater evaluation, to maximize the smoothness of the surface of generated segmentation masks and reduce false positive branch points during centerline extraction; thereby leading to higher fidelity rendering of microvascular networks. Graph generation was greatly facilitated by computing the union of the vascular segmentation masks across all time points as it enabled tracing of capillaries that had stalls at the individual time points (since the accompanying loss of the fluorescent label otherwise resulted in graph discontinuities).

Network morphological properties at baseline were in line with prior work. The vascular length density measured from fixed tissue ranged from 0.44 to 1.10 m/mm^3 [66], [76]–[80]. Our reported vascular density in the forelimb region of the primary somatosensory cortex was 0.40 ± 0.22 m/mm^3, with the low end of the range value expected due to fluorescence absorption by hemoglobin in the large pial vessels leading to signal dropout (or shadowing) in the underlying tissue. Our reported average capillary radius of 2.19 ± 1.66 μm was also in line with other studies, where the mean capillary radius ranged from 1.75 to 2.2 μm as measured with confocal microscopy or 2PFM [7], [66].

In Situ Changes to Vessel Calibers Upon Neuronal Activation

Caliber changes at individual vertices along vessel centerlines exhibited significant heterogeneity. Such heterogeneity is expected due to non-uniformly distributed alpha smooth muscle actin-containing cells along vessel walls, as well as differential activations leading to heterogeneous metabolic demand within the tissue [1], [6], [81]–[84]. Many previous studies assumed vessel caliber changes to be uniform, compromising the accuracy of the estimates.

As expected, the control 552 nm stimulation led to minimal changes in vessel calibers. To probe for off-target effects, non-transgenic mice were also tested with the same optical setup and photostimulation, with no changes to vascular diameters observed at any of the photostimulation powers utilized (data not shown). In transgenic mice, we detected an average capillary dilation in significantly responding vessels of 70±83% with low-intensity 458 nm stimulation, and 67±61% with higher intensity 458 nm stimulation. Across photostimulation conditions, the capillary dilations ranged from 2% to 805%. These calibre changes were higher than those previously reported, which varied from 2% to 20% depending on the capillary branch order [6], [7], [23], [85], [86]. Far less data are available on constrictions. In the current work, constrictions averaged 47±20% for lower-intensity blue light stimulation and 47±17% for higher-intensity blue light stimulation, with a constriction range of 5% to 97% of the baseline radius. These are higher than the previously reported constrictions of 20% [6], [23], likely due to our identifying as responding vessels only those whose caliber changed by at least twice their baseline caliber variation.

458-nm photostimulation caused capillaries to dilate when pyramidal neurons were close, and constrict when they were further away. However, the stronger blue light stimulation led to an increased rate of constrictions, double that of the low-powered blue light stimulation. For larger vessels, both 458 nm stimulation powers led to a similar dilation level that diminished with increasing distance from activated pyramidal neurons. This tendency for vessels close to neurons to dilate and further away ones to constrict would be expected in flow redirection into regions of high level of neuronal activity. Stimulation power dependence in blood flow changes has previously been reported in optogenetic mouse models with diffuse stimulation via LED probes, and following transcranial alternating current stimulation [87], [88]. However, neither of the previously employed methods was able to discern the spatial relationship between the vascular caliber changes, or relate these changes to the distribution of the stimulated neurons.

Across all stimulations, constricting vessels tended to be located deeper than dilating vessels. As the blue light stimulation power increased, the mean depth of both constricting and dilating vessels increased, likely resulting from higher intensity light reaching pyramidal neurons deeper in the tissue [89], [90]. Our results underscore that the haemodynamic response following targeted neuronal activation is not uniformly distributed across the microvascular network: accurate neurovascular coupling assessment thus requires network-based analysis.

Vascular Network Reactivity

To study the microvascular network response as a whole, we examined the assortativity between capillary radius changes and network efficiency changes following optogenetic stimulation. These two graph theory metrics were selected as they both leverage the knowledge of the vascular network structure. Assortativity sheds light on how the vascular network coordinates its responses, while efficiency provides insight into the extent to which those changes facilitate flow through the network. The assortativity revealed that as the stimulation power increased, the tendency of vessels to match their changes to those of their neighbours increased. Previously characterized assortative mechanisms include endothelial cell cation conduction via Kir2.1 channels to synchronize vascular responses [65], and spatial adjacency of pericytes on in vitro retinal preparation leading to assortative changes in neighbouring capillaries [81]. Disassortative (causing opposite changes) mechanisms of capillary coordination have also previously been observed in situ and may result from intercapillary nanotubules' signalling causing connected pericytes to undergo opposing changes [24]. While not ruling out the presence of disassortative control mechanisms, our results suggest that assortative mechanisms dominate capillary responses to neuronal activation in the somatosensory cortex.

The network efficiency here can be thought of as paralleling mean transit time, i.e., the time it takes blood to traverse the capillary network from the arteries to the veins. In situ studies of mean transit time have revealed a high heterogeneity of plasma traversal of the capillary bed during stimulation, with stimulation reducing plasma transit times by 11% to 20% from its resting levels [86], [91], and simulations suggesting that capillary network geometry and locations of caliber changes exert a substantial influence on these responses [92]. The efficiency of the vascular network here increased significantly only with the strongest 458 nm stimulation. Small dilatations may thus not increase flow in the cortex. The differences in efficiency are likely due to the patterns of localized dilations and constrictions within the vascular network. Efficiency calculations are sensitive to bottlenecks when traversing meshes and certain locations constricting or dilating can have profound impacts on the shortest paths between nodes and the path's resistivity. The highest powered 458 nm stimulation increasing efficiency may have resulted from increased assortativity causing dilation in key locations within the microvascular network, leading to a significant reduction in shortest path resistivity.

Pipeline Limitations and Adaptability

The segmentation model was trained only on vascular and neuronal labels, limiting its generalizability to segmenting alternative cells in the current state. However, it can easily be fine-tuned or retrained to label other brain cells (e.g., pericytes, astrocytes, or endothelial cells). In addition, the segmentation model performed poorly when significant bleeding occurred in the cranial window, compromising the vascular contrast. Our imaging protocol was challenged by the need to resolve individual vessel responses and capture the entire network within the span of the microvascular response to stimulation: we could thus not comment on the temporal evolution of the microvascular response. The temporal evolution of the vascular response in individual vessels, however, has been reported on already using line scanning acquisitions to measure red blood cell velocity and flux [6], [9], [23], [30], [32], [86]. Moreover, the present analysis pipeline can readily be applied to 2PFM data obtained with finer temporal (e.g., via a Piezo objective positioner) or spatial resolution, and/or larger fields of view. Finally, microvascular

networks in different brain areas may show distinct spatiotemporal profiles of response to neuronal activation. Future work is required to test the generalizability of present findings across different brain regions.

6 Conclusion

We developed a novel deep learning-based computational pipeline for analysis of a time series of 3D 2PFM images and investigation of spatial patterns in microvascular network reactivity to neuronal activation. The microvascular network was represented as a graph, allowing for the evaluation of network geometry changes over time. We tracked the size of blood vessels throughout the network and related vessel radius changes to the distance from the stimulated neurons and the cortical depth. Neuronal activation induced both dilatations and constrictions of capillaries, and the magnitude of these responses increased with increased photostimulation levels while showing significant heterogeneity within and between vessels. In the analysis presented, vertex-wise measurements were aggregated for vessel-wise analysis resulting in highly robust estimates of vessels' calibers and allowing ready comparisons to literature. Notwithstanding, the pipeline also affords vertex-wise analysis and thus registration of microvascular reactivity with other local morphological features, at an unprecedented spatial scale. With increasing distance of the vessel from the most proximal activated neuron, dilatation magnitude decreased and the incidence of constrictions increased. At the highest stimulation level investigated, the incidence of vessel constrictions also increased with cortical depth. With increasing activation levels, capillaries displayed diameter changes that were similar to their immediate neighbours, while vascular network efficiency increased only under the strongest stimulation. Our computational analysis pipeline permits probing microvascular network reactivity and sheds light on the heterogeneity and coordination of vessel caliber changes across the microvascular network.The pipeline will be made available to the research community to propel future studies of neurovascular coupling and network reactivity.

Author contributions

M.W.R. contributed to experimental conceptualization and design, surgical preparation, imaging and data acquisition, pipeline development, data analysis, and manuscript preparation. J.R.M. contributed to the experimental design conceptualization and manuscript preparation. A.A. contributed to pipeline development and manuscript preparation. A.D. contributed to surgical preparation and manuscript preparation. M.G. and B.S. contributed to funding acquisition, experimental conceptualization and design, data analysis, manuscript preparation, and supervised all aspects of the study.

Acknowledgements

We are grateful to Calcul Québec and the Digital Research Alliance of Canada (*alliancecan.ca*) for their allocation of compute resources that in part supported this research. This work was supported by funding from Canadian Institute of Health Research grants PJT376309, PJT156179 and PJT178059. M.W.R was supported by the Queen Elizabeth II/Sunnybrook and Women's College Health Sciences Centre Graduate Scholarships in Science and Technology. B.S. and M.G. are supported by the Canada Research Chair program (CRC-2018-00042 and CRC-2021-00374).

Data and code availability statement

Data are available upon request, and the code will be made available at a later date as part of a later release of the MIRACL pipeline.

Conflicts of interest

The authors do not have any conflicts of interest regarding this manuscript, its preparation, or the research that went into it.

References

[1] Iadecola C. (2017) **The Neurovascular Unit Coming of Age: A Journey through Neurovascular Coupling in Health and Disease** *Neuron* **96**:17–42 https://doi.org/10.1016/j.neuron.2017.07.030

[2] Kisler K., Nelson A. R., Montagne A., Zlokovic B. V. (2017) **Cerebral blood flow regulation and neurovascular dysfunction in Alzheimer disease** *Nat. Rev. Neurosci* **18** https://doi.org/10.1038/nrn.2017.48

[3] Kenney K., et al. (2016) **Cerebral Vascular Injury in Traumatic Brain Injury** *Exp. Neurol* **275**:353–366 https://doi.org/10.1016/j.expneurol.2015.05.019

[4] Phillips A. A., Chan F. H., Zheng M. M. Z., Krassioukov A. V., Ainslie P. N. (2016) **Neurovascular coupling in humans: Physiology, methodological advances and clinical implications** *J. Cereb. Blood Flow Metab* **36**:647–664 https://doi.org/10.1177/0271678x15617954

[5] Secomb T. W., Hsu R., Beamer N. B., Coull B. M. (2000) **Theoretical simulation of oxygen transport to brain by networks of microvessels: effects of oxygen supply and demand on tissue hypoxia** *Microcirc. N. Y. N 1994* **7**:237–247

[6] Hartmann D. A., et al. (2021) **Brain capillary pericytes exert a substantial but slow influence on blood flow** *Nat. Neurosci* :1–13

[7] Hall C. N., et al. (2014) **Capillary pericytes regulate cerebral blood flow in health and disease** *Nature* **508**:55–60 https://doi.org/10.1038/nature13165

[8] Mester J. R., et al. (2021) **Attenuation of tonic inhibition prevents chronic neurovascular impairments in a Thy1-ChR2 mouse model of repeated, mild traumatic brain injury** *Theranostics* **11**:7685–7699 https://doi.org/10.7150/thno.60190

[9] Adams C., et al. (2018) **Neurogliovascular dysfunction in a model of repeated traumatic brain injury** *Theranostics* **8**:4824–4836 https://doi.org/10.7150/thno.24747

[10] Carroll W. J., Maganti N., Gill M. K. (2020) **Hypoperfusion of the deep capillary plexus associated with acute on chronic cocaine use** *Am. J. Ophthalmol. Case Rep* **18** https://doi.org/10.1016/j.ajoc.2020.100684

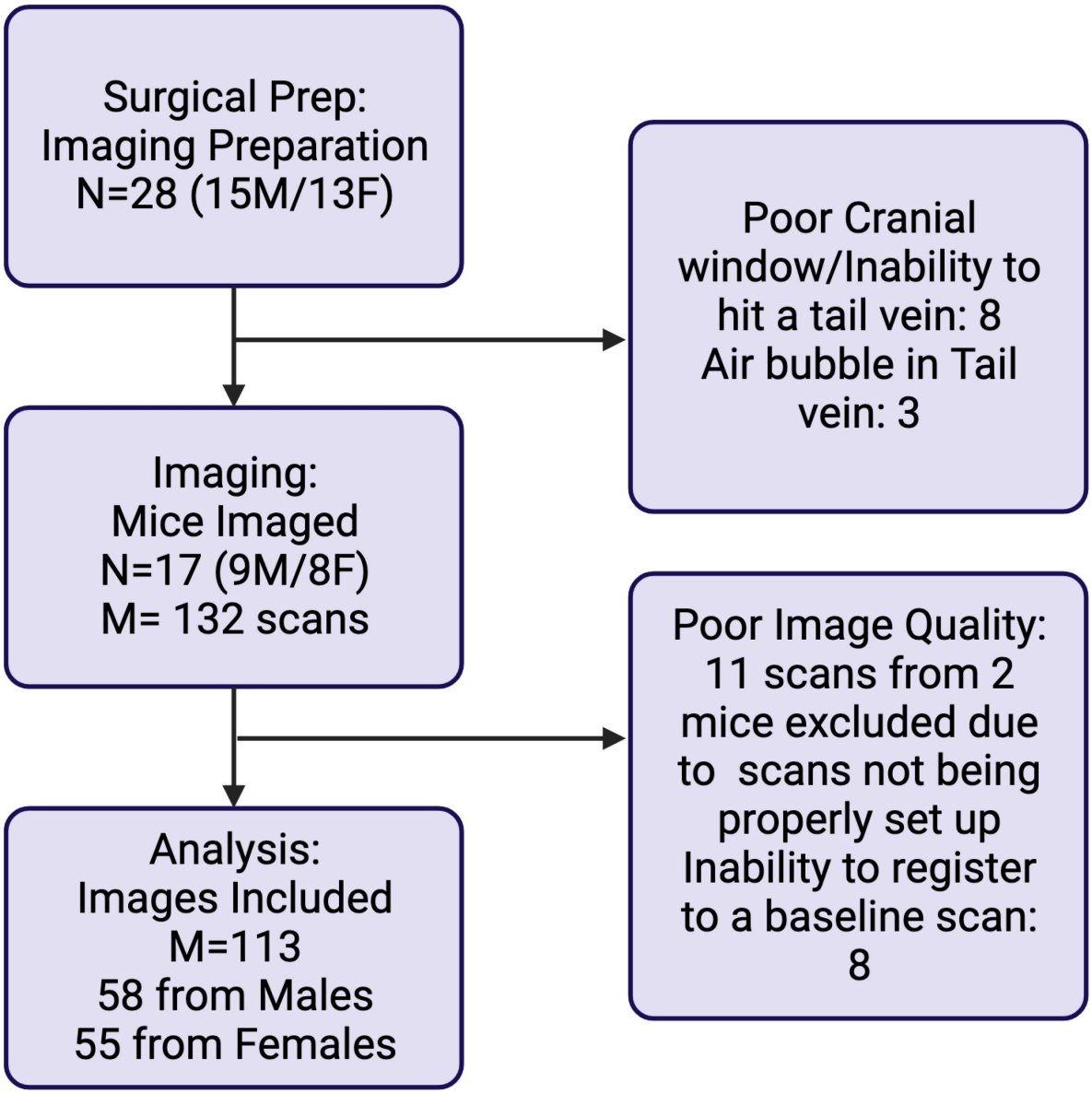

Supplementary Figure 1.

Attrition:

Flow chart of animal numbers at each step of the experiment.

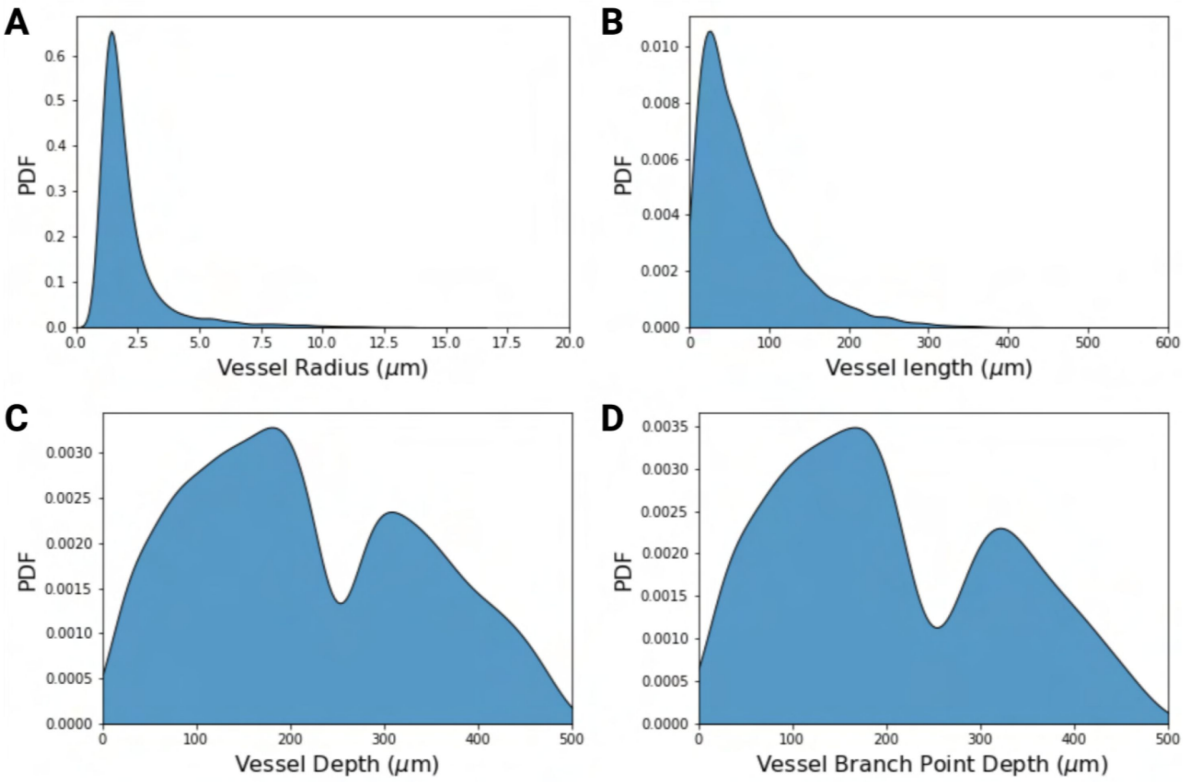

Supplementary Figure 2.

Vascular Network Characteristics:

A. Probability density of the extracted mean radii of vascular segments. **B.** Probability density of the lengths of extracted vessel segments between branch points or terminal ends. **C.** Probability density of the mean vessel segment depths. **D.** Probability density of the depths of vessel branch points. Terminal nodes were excluded from this probability density. 12555 vessels, and 6421 vascular junctions from 17 mice (9M/8F) were used to estimate these PDFs.

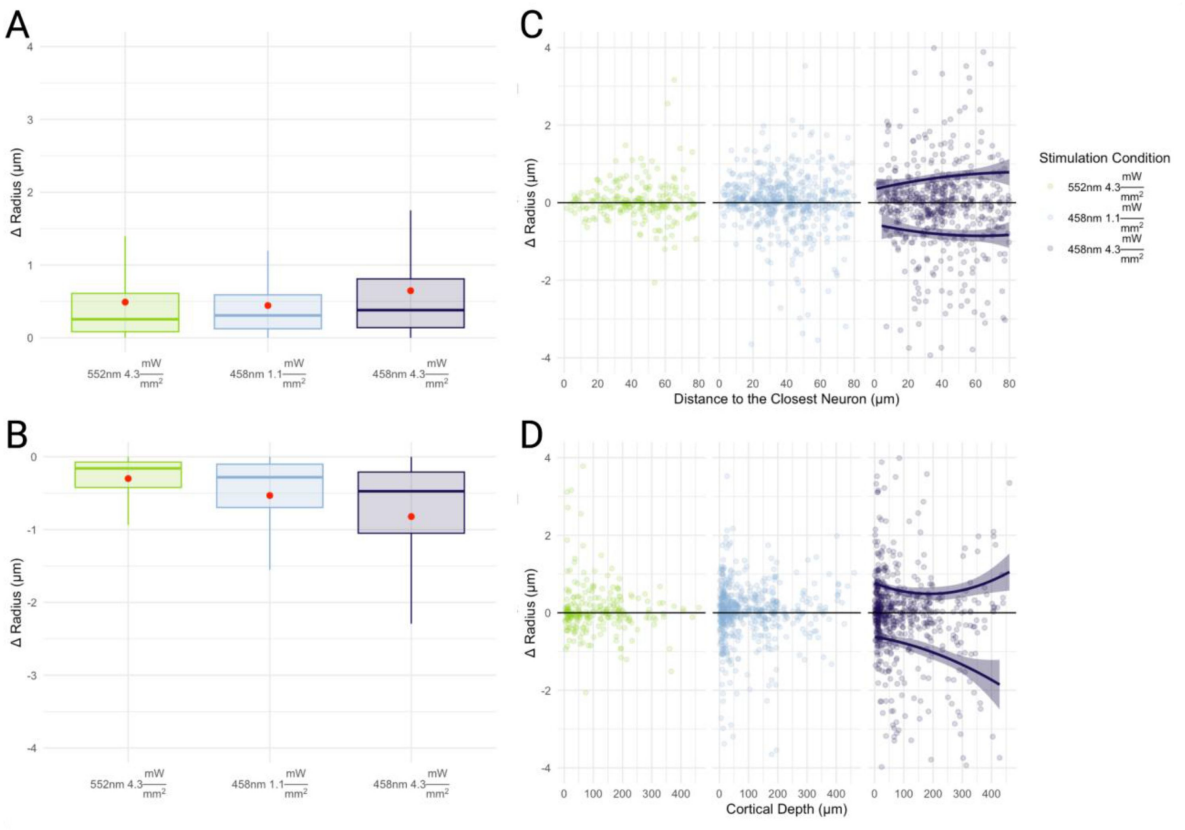

Supplemental Figure 3.

Large Vessels Radius Changes Following Optogenetic Stimulation:

All vascular responses in large vessels (radius > 5μm) separated into dilators **A.** and constrictors **B.** showing an increase in the magnitude of response as stimulation power increases. **C.** Radius changes to vascular radii in relation to the closest pyramidal neurons (within 80 μm). **D.** Mean depth of responding large vessels.

	Mean Across Subjects During Imaging
End-tidal pCO2	15.93 ± 5.07 mmHg
Heart rate	318.30 ± 28.69 BPM
O2 Saturation	96.30 ± 3.50 %
Breath Rate	123.89 ± 12.47 BPM
Temperature	37.15 ± 0.30 °C
Weight	27.94 ± 6.03 g

Supplementary Table 1

Physiological Monitoring Data

Category	Transformation	Parameters
Cropping	Random spatial cropping	Crops: 8 Crop size: 128x128x128
Rotations	Random rotation 90 degrees	Max rotations: 3
Mirroring	Random flipping	Axes: all
Rotations	Random affine transformation	Rotation restriction: 20°
Zoom	Random zooming	Min zoom: 0.3 Max zoom: 3
Deformations	Random 3D elastic deformation	Sigma: 1 and 3 SU Magnitude: 3-15 µm
	Random grid distortion	Cells: 8 Magnitude: -0.3 to 0.3 of cell width
Intensity Transformations	Random intensity shift	Offset: 0.4 SU
	Random contrast adjustment	Gamma: 0.5 to 5.5
	Random histogram shift	Control points: 4
Gaussian Transformation	Random Gaussian sharpening	Sigma1: 0.5 to 1 SU Sigma2: 0.5 SU Alpha: 10 to 30 SU
	Random Gaussian smoothing	Sigma: 0.25 to 1.25 SU
	Random Gaussian noise	Mean : 0 SU STD: 0.2 SU
Drop pixels	Random coarse dropout	Minimum holes: 50 Maximum holes: 1000 Spatial size: 2 pixels Fill: 0.0001 to 0.1 SU

Supplementary Table 2

Data Augmentations:

	UNETR	UNet	Ilastik
Vessels			
Dice	0.763±0.096	0.790±0.088	0.449±0.375
Precision	0.811±0.089	0.813±0.076	0.377±0.347
Recall	0.750±0.172	0.797±0.165	0.893±0.198
Hausdorff 95%	13.567±12.131	12.116±12.144	38.921±35.706
Mean Surface Distance	1.900±1.545	1.737±1.622	1.675±1.355
Neurons			
Dice	0.712±0.062	0.766±0.044	0.487±0.196
Precision	0.628±0.111	0.698±0.091	0.435±0.239
Recall	0.841±0.053	0.860±0.061	0.814±252
Hausdorff 95%	23.654±19.299	20.340±22.67	50.000±26.660
Mean Surface Distance	1.248±0.569	2.409±3.901	4.450±7.315

Supplementary Table 3

Model performance comparisons:

[11] Yang Q., et al. (2022) **Cerebral small vessel disease alters neurovascular unit regulation of microcirculation integrity involved in vascular cognitive impairment** *Neurobiol. Dis* **170** https://doi.org/10.1016/j.nbd.2022.105750

[12] Mayer A. R., Mannell M. V., Ling J., Gasparovic C., Yeo R. A. (2011) **Functional connectivity in mild traumatic brain injury** *Hum. Brain Mapp* **32**:1825–1835 https://doi.org/10.1002/hbm.21151

[13] Park E., Bell J. D., Siddiq I. P., Baker A. J. (2009) **An analysis of regional microvascular loss and recovery following two grades of fluid percussion trauma: a role for hypoxia-inducible factors in traumatic brain injury** *J. Cereb. Blood Flow Metab. Off. J. Int. Soc. Cereb. Blood Flow Metab* **29**:575–584 https://doi.org/10.1038/jcbfm.2008.151

[14] Petkus V., Krakauskaitė S., Preikšaitis A., Ročka S., Chomskis R., Ragauskas A. (2016) **Association between the outcome of traumatic brain injury patients and cerebrovascular autoregulation, cerebral perfusion pressure, age, and injury grades** *Medicina (Mex* **52**:46–53 https://doi.org/10.1016/j.medici.2016.01.004

[15] Ramos-Cejudo J., et al. (2018) **Traumatic Brain Injury and Alzheimer's Disease: The Cerebrovascular Link** *EBioMedicine* **28**:21–30 https://doi.org/10.1016/j.ebiom.2018.01.021

[16] Franzmeier N., et al. (2019) **Functional connectivity associated with tau levels in ageing, Alzheimer's, and small vessel disease** *Brain* **142**:1093–1107 https://doi.org/10.1093/brain/awz026

[17] Rabin J. S., et al. (2019) **Vascular Risk and β -Amyloid Are Synergistically Associated with Cortical Tau: Vascular Risk, Aβ, and Tau** *Ann. Neurol* **85**:272–279 https://doi.org/10.1002/ana.25399

[18] Boehme N. A., et al. (2021) **Axonopathy precedes cell death in ocular damage mediated by blast exposure** *Sci. Rep* **11** https://doi.org/10.1038/s41598-021-90412-2

[19] Koliatsos V. E., Rao V. (2020) **The Behavioral Neuroscience of Traumatic Brain Injury** *Psychiatr. Clin. North Am* **43**:305–330 https://doi.org/10.1016/j.psc.2020.02.009

[20] Ware J. B., et al. (2020) **Relationship of Cerebral Blood Flow to Cognitive Function and Recovery in Early Chronic Traumatic Brain Injury** *J. Neurotrauma* **37**:2180–2187 https://doi.org/10.1089/neu.2020.7031

[21] Hill R. A., Tong L., Yuan P., Murikinati S., Gupta S., Grutzendler J. (2015) **Regional Blood Flow in the Normal and Ischemic Brain Is Controlled by Arteriolar Smooth Muscle Cell Contractility and Not by Capillary Pericytes** *Neuron* **87**:95–110 https://doi.org/10.1016/j.neuron.2015.06.001

[22] Lindvere L., Dorr A., Stefanovic B. (2010) **Two-photon fluorescence microscopy of cerebral hemodynamics** *Cold Spring Harb. Protoc* **2010** https://doi.org/10.1101/pdb.prot5494

[23] O'Herron P. J., Hartmann D. A., Xie K., Kara P., Shih A. Y. (2022) **3D optogenetic control of arteriole diameter in vivo** *eLife* **11** https://doi.org/10.7554/eLife.72802

[24] Alarcon-Martinez L., et al. (2020) **Interpericyte tunnelling nanotubes regulate neurovascular coupling** *Nature* **585**:91–95 https://doi.org/10.1038/s41586-020-2589-x

[25] Sakadžić S., et al. (2011) **Cerebral blood oxygenation measurement based on oxygen-dependent quenching of phosphorescence** *J. Vis. Exp. JoVE* **51** https://doi.org/10.3791/1694

[26] Guo Y., et al. (2023) **Dynamic Volumetric Imaging of Mouse Cerebral Blood Vessels In Vivo with an Ultralong Anti-Diffracting Beam** *Molecules* **28** https://doi.org/10.3390/molecules28134936

[27] Giblin J. T., et al. (2023) **Measuring capillary flow dynamics using interlaced two-photon volumetric scanning** *J. Cereb. Blood Flow Metab* **43**:595–609 https://doi.org/10.1177/0271678x221145091

[28] McDowell K. P., Berthiaume A.-A., Tieu T., Hartmann D. A., Shih A. Y. (2021) **VasoMetrics: unbiased spatiotemporal analysis of microvascular diameter in multi-photon imaging applications** *Quant. Imaging Med. Surg* **11**:969–982 https://doi.org/10.21037/qims-20-920

[29] Kim G., et al. (2023) **Direct Blood Cell Flow Imaging in Microvascular Networks** *Small* https://doi.org/10.1002/smll.202302244

[30] Mester J. R., et al. (2019) **In vivo neurovascular response to focused photoactivation of Channelrhodopsin-2** *NeuroImage* **192**:135–144 https://doi.org/10.1016/j.neuroimage.2019.01.036

[31] Kim T. N., et al. (2012) **Line-Scanning Particle Image Velocimetry: An Optical Approach for Quantifying a Wide Range of Blood Flow Speeds in Live Animals** *PLOS ONE* **7** https://doi.org/10.1371/journal.pone.0038590

[32] Kleinfeld D., Mitra P. P., Helmchen F., Denk W. (1998) **Fluctuations and stimulus-induced changes in blood flow observed in individual capillaries in layers 2 through 4 of rat neocortex** *Proc. Natl. Acad. Sci. U. S. A* **95**:15741–15746 https://doi.org/10.1073/pnas.95.26.15741

[33] Boyden E. S., Zhang F., Bamberg E., Nagel G., Deisseroth K. (2005) **Millisecond-timescale, genetically targeted optical control of neural activity** *Nat. Neurosci* **8**:1263–1268 https://doi.org/10.1038/nn1525

[34] Arenkiel B. R., et al. (2007) **In vivo light-induced activation of neural circuitry in transgenic mice expressing channelrhodopsin-2** *Neuron* **54**:205–218 https://doi.org/10.1016/j.neuron.2007.03.005

[35] du Sert N. P., et al. (2020) **Reporting animal research: Explanation and elaboration for the ARRIVE guidelines 2.0** *PLOS Biol* **18** https://doi.org/10.1371/journal.pbio.3000411

[36] Lin J. Y., Lin M. Z., Steinbach P., Tsien R. Y. (2009) **Characterization of Engineered Channelrhodopsin Variants with Improved Properties and Kinetics** *Biophys. J* **96**:1803–1814 https://doi.org/10.1016/j.bpj.2008.11.034

[37] Rungta R. L., Osmanski B.-F., Boido D., Tanter M., Charpak S. (2017) **Light controls cerebral blood flow in naive animals** *Nat. Commun* **8** https://doi.org/10.1038/ncomms14191

[38] Lambert T. J. (2019) **FPbase: a community-editable fluorescent protein database** *Nat. Methods* **16** https://doi.org/10.1038/s41592-019-0352-8

[39] Consortium M. (2022) **"MONAI: Medical Open Network for AI." Zenodo** *Jul* **25** https://doi.org/10.5281/zenodo.6903385

[40] Hatamizadeh A., et al. (2021) **UNETR: Transformers for 3D Medical Image Segmentation** *ArXiv210310504 Cs Eess*

[41] Kerfoot E., Clough J., Oksuz I., Lee J., King A. P., Schnabel J. A. (2019) **"Left-Ventricle Quantification Using Residual U-Net," in Statistical Atlases and Computational Models of the Heart. Atrial Segmentation and LV Quantification Challenges, M. Pop, M. Sermesant, J. Zhao, S. Li, K. McLeod, A. Young, K. Rhode, and T. Mansi** *Eds., in Lecture Notes in Computer Science. Cham: Springer International Publishing* :371–380 https://doi.org/10.1007/978-3-030-12029-0_40

[42] Srivastava N., Hinton G., Krizhevsky A., Sutskever I., Salakhutdinov R. (2014) **Dropout: A Simple Way to Prevent Neural Networks from Overfitting** *J. Mach. Learn. Res* **15**:1929–1958

[43] Mojiri Forooshani P., et al. (2022) **Deep Bayesian networks for uncertainty estimation and adversarial resistance of white matter hyperintensity segmentation** *Hum. Brain Mapp* **43**:2089–2108 https://doi.org/10.1002/hbm.25784

[44] Ulyanov D., Vedaldi A., Lempitsky V. (2017) **Instance Normalization: The Missing Ingredient for Fast Stylization** *arXiv* https://doi.org/10.48550/arXiv.1607.08022

[45] He K., Zhang X., Ren S., Sun J. (2015) **"Delving Deep into Rectifiers: Surpassing Human-Level Performance on ImageNet Classification." arXiv** *Feb* **6** https://doi.org/10.48550/arXiv.1502.01852

[46] He K., Zhang X., Ren S., Sun J. (2016) **"Identity Mappings in Deep Residual Networks." arXiv** *Jul* **25** https://doi.org/10.48550/arXiv.1603.05027

[47] Zhang Z., Liu Q., Wang Y. (2018) **Road Extraction by Deep Residual U-Net** *IEEE Geosci. Remote Sens. Lett* **15**:749–753 https://doi.org/10.1109/LGRS.2018.2802944

[48] Goubran M., et al. **Hippocampal segmentation for brains with extensive atrophy using three-dimensional convolutional neural networks** *Hum. Brain Mapp* **41**:291–308 https://doi.org/10.1002/hbm.24811

[49] Salehi S. S. M., Erdogmus D., Gholipour A. (2017) **Tversky loss function for image segmentation using 3D fully convolutional deep networks** *arXiv* https://doi.org/10.48550/arXiv.1706.05721

[50] Lin T.-Y., Goyal P., Girshick R., He K., Dollár P. (2018) **Focal Loss for Dense Object Detection** *arXiv* https://doi.org/10.48550/arXiv.1708.02002

[51] Kingma D. P., Ba J. (2017) **Adam: A Method for Stochastic Optimization** *arXiv* https://doi.org/10.48550/arXiv.1412.6980

[52] Berg S., et al. (2019) **ilastik: interactive machine learning for (bio)image analysis** *Nat. Methods* **16** https://doi.org/10.1038/s41592-019-0582-9

[53] VIGRA **"VIGRA Homepage." Accessed: Aug. 30, 2023. [Online]. Available: https://ukoethe.github.io/vigra/**

[54] Avants B. B., Tustison N. J., Stauffer M., Song G., Wu B., Gee J. C. (2014) **The Insight ToolKit image registration framework," Front** *Neuroinformatics* **8** https://doi.org/10.3389/fninf.2014.00044

[55] Gal Y., Ghahramani Z. (2016) **Dropout as a Bayesian Approximation: Representing Model Uncertainty in Deep Learning** *ArXiv150602142 Cs Stat*

[56] Lee T. C., Kashyap R. L., Chu C. N. (1994) **Building Skeleton Models via 3-D Medial Surface Axis Thinning Algorithms** *CVGIP Graph. Models Image Process* **56**:462–478 https://doi.org/10.1006/cgip.1994.1042

[57] Nunez-Iglesias J., Blanch A. J., Looker O., Dixon M. W., Tilley L. (2018) **A new Python library to analyse skeleton images confirms malaria parasite remodelling of the red blood cell membrane skeleton** *PeerJ* **6** https://doi.org/10.7717/peerj.4312

[58] Newman M. E. J. (2003) **Mixing patterns in networks," Phys** *Rev. E* **67** https://doi.org/10.1103/PhysRevE.67.026126

[59] Nader E., et al. (2019) **Blood Rheology: Key Parameters, Impact on Blood Flow, Role in Sickle Cell Disease and Effects of Exercise** *Front. Physiol* **10** https://doi.org/10.3389/fphys.2019.01329

[60] Schaffer C. B., et al. (2006) **Two-Photon Imaging of Cortical Surface Microvessels Reveals a Robust Redistribution in Blood Flow after Vascular Occlusion** *PLOS Biol* **4** https://doi.org/10.1371/journal.pbio.0040022

[61] Virtanen P., et al. (2020) **SciPy 1.0: fundamental algorithms for scientific computing in Python** *Nat. Methods* **17** https://doi.org/10.1038/s41592-019-0686-2

[62] Bates D., et al. (2015) **Fitting Linear Mixed-Effects Models Using lme4** *Journal of Statistical Software* **67**:1–48

[63] Lenth R. V., et al. (2023) **emmeans: Estimated Marginal Means, aka Least-Squares Means** *Oct* **17**

[64] DeFelipe J., Alonso-Nanclares L., Arellano J. I. (2002) **Microstructure of the neocortex: comparative aspects** *J. Neurocytol* **31**:299–316 https://doi.org/10.1023/a:1024130211265

[65] Dabertrand F., et al. (2021) **PIP2 corrects cerebral blood flow deficits in small vessel disease by rescuing capillary Kir2.1 activity** *Proc. Natl. Acad. Sci. U. S. A* **118** https://doi.org/10.1073/pnas.2025998118

[66] Tsai P. S., et al. (2009) **Correlations of Neuronal and Microvascular Densities in Murine Cortex Revealed by Direct Counting and Colocalization of Nuclei and Vessels** *J. Neurosci* **29**:14553–14570 https://doi.org/10.1523/JNEUROSCI.3287-09.2009

[67] Rennie M. Y., et al. (2011) **Vessel tortuousity and reduced vascularization in the fetoplacental arterial tree after maternal exposure to polycyclic aromatic hydrocarbons** *Am. J. Physiol.-Heart Circ. Physiol* **300**:H675–H684 https://doi.org/10.1152/ajpheart.00510.2010

[68] Steinman J., Koletar M. M., Stefanovic B., Sled J. G. (2017) **3D morphological analysis of the mouse cerebral vasculature: Comparison of in vivo and ex vivo methods** *PLOS ONE* **12** https://doi.org/10.1371/journal.pone.0186676

[69] Lindvere L., et al. (2013) **Cerebral microvascular network geometry changes in response to functional stimulation** *NeuroImage* **71**:248–259 https://doi.org/10.1016/j.neuroimage.2013.01.011

[70] Damseh R., Cheriet F., Lesage F. (2018) **Fully Convolutional DenseNets for Segmentation of Microvessels in Two-photon Microscopy*** *2018 40th Annual International Conference of the IEEE Engineering in Medicine and Biology Society (EMBC)* :661–665 https://doi.org/10.1109/EMBC.2018.8512285

[71] Goodarzi Ardakani V., Gambaruto A. M., Silva G., Pereira R. (2022) **A porosity model for medical image segmentation of vessels** *Int. J. Numer. Methods Biomed. Eng* **38** https://doi.org/10.1002/cnm.3580

[72] Livne M., et al. (2019) **A U-Net Deep Learning Framework for High Performance Vessel Segmentation in Patients With Cerebrovascular Disease** *Front. Neurosci* **13** https://doi.org/10.3389/fnins.2019.00097

[73] Mookiah M. R. K., et al. (2021) **A review of machine learning methods for retinal blood vessel segmentation and artery/vein classification** *Med. Image Anal* **68** https://doi.org/10.1016/j.media.2020.101905

[74] Tetteh G., et al. (2020) **DeepVesselNet: Vessel Segmentation, Centerline Prediction, and Bifurcation Detection in 3-D Angiographic Volumes** *Frontiers Neuroscience* **14**

[75] Poon C., Teikari P., Rachmadi M. F., Skibbe H., Hynynen K. (2023) **A dataset of rodent cerebrovasculature from in vivo multiphoton fluorescence microscopy imaging** *Sci. Data* **10** https://doi.org/10.1038/s41597-023-02048-8

[76] Todorov M. I., et al. (2020) **Machine learning analysis of whole mouse brain vasculature** *Nat. Methods* **17** https://doi.org/10.1038/s41592-020-0792-1

[77] Boero J. A., Ascher J., Arregui A., Rovainen C., Woolsey T. A. (1999) **Increased brain capillaries in chronic hypoxia** *J. Appl. Physiol. Bethesda Md 1985* **86**:1211–1219 https://doi.org/10.1152/jappl.1999.86.4.1211

[78] Lugo-Hernandez E., et al. (2017) **3D visualization and quantification of microvessels in the whole ischemic mouse brain using solvent-based clearing and light sheet microscopy** *J. Cereb. Blood Flow Metab* **37**:3355–3367 https://doi.org/10.1177/0271678x17698970

[79] Zhang L.-Y., et al. (2018) **CLARITY for High-resolution Imaging and Quantification of Vasculature in the Whole Mouse Brain** *Aging Dis* **9**:262–272 https://doi.org/10.14336/AD.2017.0613

[80] Miettinen A., et al. (2021) **Micrometer-resolution reconstruction and analysis of whole mouse brain vasculature by synchrotron-based phase-contrast tomographic microscopy** *bioRxiv* https://doi.org/10.1101/2021.03.16.435616

[81] Kovacs-Oller T., Ivanova E., Bianchimano P., Sagdullaev B. T. (2020) **The pericyte connectome: spatial precision of neurovascular coupling is driven by selective connectivity maps of pericytes and endothelial cells and is disrupted in diabetes** *Cell Discov* **6** https://doi.org/10.1038/s41421-020-0180-0

[82] Abdelazim H., et al. (2022) **Pericyte Heterogeneity Identified by 3D Ultrastructural Analysis of the Microvessel Wall** *Cell Biology, preprint* https://doi.org/10.1101/2022.08.08.503052

[83] Quelhos P., et al. (2020) **Characterization of culture from smooth muscle cells isolated from rat middle cerebral arteries** *Tissue and Cell* **66**

[84] Wang G., Jacquet L., Karamariti E., Xu Q. (2015) **Origin and differentiation of vascular smooth muscle cells** *J. Physiol* **593**:3013–3030 https://doi.org/10.1113/JP270033

[85] Del Franco A. P., Chiang P.-P., Newman E. A. (2022) **Dilation of cortical capillaries is not related to astrocyte calcium signaling** *Glia* **70**:508–521 https://doi.org/10.1002/glia.24119

[86] Stefanovic B., et al. (2008) **Functional reactivity of cerebral capillaries** *J. Cereb. Blood Flow Metab. Off. J. Int. Soc. Cereb. Blood Flow Metab* **28**:961–972 https://doi.org/10.1038/sj.jcbfm.9600590

[87] Lee J., et al. (2021) **Opposed hemodynamic responses following increased excitation and parvalbumin-based inhibition** *J. Cereb. Blood Flow Metab* **41**:841–856 https://doi.org/10.1177/0271678x20930831

[88] Turner D. A., Degan S., Galeffi F., Schmidt S., Peterchev A. V. (2021) **Rapid, Dose-Dependent Enhancement of Cerebral Blood Flow by transcranial AC Stimulation in Mouse** *Brain Stimul. Basic Transl. Clin. Res. Neuromodulation* **14**:80–87 https://doi.org/10.1016/j.brs.2020.11.012

[89] Johnson E. L., et al. (2021) **Characterization of light penetration through brain tissue, for optogenetic stimulation** *bioRxiv* https://doi.org/10.1101/2021.04.08.438932

[90] Al-Juboori S. I., Dondzillo A., Stubblefield E. A., Felsen G., Lei T. C., Klug A. (2013) **Light scattering properties vary across different regions of the adult mouse brain** *PloS One* **8** https://doi.org/10.1371/journal.pone.0067626

[91] Gutiérrez-Jiménez E., et al. (2016) **Effect of electrical forepaw stimulation on capillary transit-time heterogeneity (CTH)** *J. Cereb. Blood Flow Metab* **36**:2072–2086 https://doi.org/10.1177/0271678x16631560

[92] Lücker A., Secomb T. W., Barrett M. J. P., Weber B., Jenny P. (2018) **The Relation Between Capillary Transit Times and Hemoglobin Saturation Heterogeneity. Part 2: Capillary Networks** *Front. Physiol* **9** https://doi.org/10.3389/fphys.2018.01296

Article and author information

Matthew Rozak
Department of Medical Biophysics, University of Toronto, Toronto, Ontario, Canada, Physical Sciences, Sunnybrook Research Institute, Toronto, Ontario, Canada
For correspondence: matthew.rozak@mail.utoronto.ca
ORCID iD: 0009-0001-5604-1405

James Mester
Department of Medical Biophysics, University of Toronto, Toronto, Ontario, Canada, Physical Sciences, Sunnybrook Research Institute, Toronto, Ontario, Canada

Ahmadreza Attarpour
Department of Medical Biophysics, University of Toronto, Toronto, Ontario, Canada, Physical Sciences, Sunnybrook Research Institute, Toronto, Ontario, Canada

Adrienne Dorr
Physical Sciences, Sunnybrook Research Institute, Toronto, Ontario, Canada

Maged Goubran
Department of Medical Biophysics, University of Toronto, Toronto, Ontario, Canada, Physical Sciences, Sunnybrook Research Institute, Toronto, Ontario, Canada, Hurvitz Brain Sciences, Sunnybrook Research Institute, Toronto, Ontario, Canada
ORCID iD: 0000-0001-5880-0818

Bojana Stefanovic
Department of Medical Biophysics, University of Toronto, Toronto, Ontario, Canada, Physical Sciences, Sunnybrook Research Institute, Toronto, Ontario, Canada, Hurvitz Brain Sciences, Sunnybrook Research Institute, Toronto, Ontario, Canada
For correspondence: bojana.stefanovic@utoronto.ca

Copyright

Editors

Reviewing Editor
Jason Lerch
University of Oxford, Oxford, United Kingdom

Senior Editor
Panayiota Poirazi
FORTH Institute of Molecular Biology and Biotechnology, Heraklion, Greece

Reviewer #1 (Public Review):

Summary:

In this manuscript, the authors describe a new pipeline to measure changes in vasculature diameter upon opt-genetic stimulation of neurons.

The work is interesting and the topic is quite relevant to better understand the hemodynamic response on the graph/network level.

Strengths:

The manuscript provides a pipeline that allows for the detection of changes in the vessel diameter as well as simultaneously allowing for the location of the neurons driven by stimulation.

The resulting data could provide interesting insights into the graph-level mechanisms of regulating activity-dependent blood flow.

The interesting findings include that vessel radius changes depend on depth from the cortical surface and that dilations on average happen closer to the activated neurons.

Weaknesses:

The utility of a pipeline depends on the generalization properties.

While the proposed pipeline seems to work for the data the authors acquired, it is unclear if this pipeline will actually generalize to novel data sets possibly recorded by a different microscope (e.g. different brand), or different imagining conditions (e.g. illumination or different imagining artifacts) or even to different brain regions or animal species, etc.

The authors provide a 'black-box' approach that might work well for their particular data sets and image acquisition settings but it is left unclear how this pipeline is actually widely applicable to other conditions as such data is not provided.

In my experience, without well-defined image pre-processing steps and without training on a wide range of image conditions pipelines typically require significant retraining, which in turn requires generating sufficient amounts of training data, partly defying the purpose of the pipeline.

It is unclear from the manuscript, how well this pipeline will perform on novel data possibly recorded by a different lab or with a different microscope.

Analysis

Some of the chosen analysis results seem to not fully match the shown data, or the visualization of the data is hard to interpret in the current form. Additionally, some measures seem not fully adapted to the current situation (e.g. the efficiency measure does not consider possible sources or sinks). Thus, some additional analysis work might be required to account for this.

https://doi.org/10.7554/eLife.95525.1.sa1

Reviewer #2 (Public Review):

Summary:

The authors develop a highly detailed pipeline to analyze hemodynamic signals from in vivo two-photon fluorescence microscopy. This includes motion correction, segmentation of the vascular network, diameter measurements across time, mapping neuronal position relative to the vascular network, and analyzing vascular network properties (interactions between different vascular segments). For the segmentation, the authors use a Convolution Neural Network to identify vessel (or neural) and background pixels and train it using ground truth images based on semi-automated mapping followed by human correction/annotation. Considerable processing was done on the segmented images to improve accuracy, extract vessel center lines, and compute frame-by-frame diameters. The model was tested with artificial diameter increases and Gaussian noise and proved robust to these manipulations.

Network-level properties include Assortativity - a measure of how similar a vessel's response is to nearby vessels - and Efficiency - the ease of flow through the network (essentially, the combined resistance of a path based on diameter and vessel length between two points).

Strengths:

This is a very powerful tool for cerebral vascular biologists as many of these tasks are labor intensive, prone to subjectivity, and often not performed due to the complexity of collecting and managing volumes of vascular signals. Modelling is not my specialty so I cannot speak too specifically, but the model appears to be well-designed and robust to perturbations. It has many clever features for processing the data.

The authors rightly point out that there is a real lack in the field of knowledge of vascular network activity at single-vessel resolution. Network anatomy has been studied, but hemodynamics are typically studied either with coarse resolution or in only one or a few vessels at a time. This pipeline has the potential to change that.

Weaknesses:

The authors apply their method to in vivo data. However, there are some weaknesses in the design that make it hard to accept many of the conclusions and even to see that the method could yield much useful data with this type of application. Primarily, the acquisition of a large volume of tissue is very slow. In order to obtain a network of vascular activity, large volumes are imaged with high resolution. However, the volumes are scanned once every 42 seconds following stimulation. Most vascular responses to neuronal activation have come and gone in 42 seconds so each vessel segment is only being sampled at a single time point in the vascular response. So all of the data on diameter changes are impossible to compare since some vessels are sampled during the initial phase of the vascular response, some during the decay, and many probably after it has already returned to baseline. The authors attempt to overcome this by alternating the direction of the scan (from surface to deep and vice versa). But this only provides two sample points along the vascular response curve and so the problem still remains.

A second problem is the use of optogenetic stimulation to activate the tissue. First, it has been shown that blue light itself can increase blood flow (Rungta et al 2017). The authors note the concern about temperature increases but that is not the same issue. The discussion mentions that non-transgenic mice were used to control for this with "data not shown". This is very important data given these earlier reports that have found such effects and so should be included. Secondly, there doesn't seem to be any monitoring of neural activity following the photo-stimulation. The authors repeatedly mention "activated" neurons and claim that vessel properties change based on distance from "activated" neurons. But I can't find anything to suggest that they know which neurons were active versus just labeled. Third, the stimulation laser is focused at a single depth plane. Since it is single-photon excitation, there is likely a large volume of activated neurons. But there is no way of knowing the spatial arrangement of neural activity and so again, including this as a factor in the analysis of vascular responses seems unjustified.

The study could also benefit from more clear illustration of the quality of the model's output. It is hard to tell from static images of 3-D volumes how accurate the vessel segmentation is. Perhaps some videos going through the volume with the masks overlaid would provide some clarity. Also, a comparison to commercial vessel segmentation programs would be useful in addition to benchmarking to the ground truth manual data.

Another useful metric for the model's success would be the reproducibility of the vessel responses. Seeing such a large number of vessels showing constrictions raises some flags and so showing that the model pulled out the same response from the same vessels across multiple repetitions would make such data easier to accept.

A number of findings are questionable, at least in part due to these design properties.

There are unrealistically large dilations and constrictions indicated. These are likely due to artifacts of the automated platform. Inspection of these results by eye would help understand what is going on.

In Figure 6, there doesn't seem to be much correlation between vessels with large baseline level changes and vessels with large stimulus-evoked changes. It would be expected that large arteries would have a lot of variability in both conditions and veins much less. There is also not much within-vessel consistency. For instance, the third row shows what looks like a

surface vessel constricting to stimulation but a branch coming off of it dilating - this seems biologically unrealistic.

As mentioned, the large proportion of constricting capillaries is not something found in the literature. Do these happen at a certain time point following the stimulation? Did the same vessel segments show dilation at times and constriction at other times? In fact, the overall proportion of dilators and constrictors is not given. Are they spatially clustered? The assortativity result implies that there is some clustering, and the theory of blood stealing by active tissue from inactive tissue is cited. However, this theory would imply a region where virtually all vessels are dilating and another region away from the active tissue with constrictions. Was anything that dramatic seen?

As mentioned, the claims about distance to active neurons are not meaningful if there is no measure of which neurons were active and which weren't. But even still, the claim is overly strong as the average distance to the nearest neuron for dilators was ~17 microns and for constrictors it was ~22 microns - about a half a neuronal soma difference.

The distance to the nearest neuron likely will depend on depth as well - neurons are quite sparse superficially and very dense in layer 4. The capillary network varies much less (see Blinder et al 2016 Nature Neuroscience). So the distance of a neuron to the nearest capillary may not vary much with depth, but the distance from the capillary to the nearest neuron might vary quite a lot.
Why were nearly all vessels > 5um diameter not responding >2SD above baseline? Did they have highly variable baselines or small responses? Usually, bigger vessels respond strongly to local neural activity.

https://doi.org/10.7554/eLife.95525.1.sa0

Author Response

We would like to thank the reviewers for providing constructive feedback on the manuscript. To address the weaknesses identified, we are performing additional experiments and generating additional data, to be added to the updated manuscript.

> *(1) The utility of a pipeline depends on the generalization properties.*
>
> *While the proposed pipeline seems to work for the data the authors acquired, it is unclear if this pipeline will actually generalize to novel data sets possibly recorded by a different microscope (e.g. different brand), or different imagining conditions (e.g. illumination or different imagining artifacts) or even to different brain regions or animal species, etc.*
>
> *The authors provide a 'black-box' approach that might work well for their particular data sets and image acquisition settings but it is left unclear how this pipeline is actually widely applicable to other conditions as such data is not provided.*
>
> *In my experience, without well-defined image pre-processing steps and without training on a wide range of image conditions pipelines typically require significant retraining, which in turn requires generating sufficient amounts of training data, partly defying the purpose of the pipeline. It is unclear from the manuscript, how well this pipeline will perform on novel data possibly recorded by a different lab or with a different microscope.*

To address generalizability, we are performing several validation experiments with data from different 1) channels, 2) species (rat), and 3) microscopes, to highlight the robustness of our

deep learning (DL) segmentation model to out-of-distribution data with different characteristics and acquisition protocols. We first used our model to segment three images (507x507 x&y, 250-170 um z) from three C57BL/6 mice acquired on the same two-photon fluorescent microscope following the same imaging protocol. The vasculature was labelled with the Texas Red dextran, as in the current experiment. In place of the EYFP signal from pyramidal neurons (2nd channel), gaussian noise was generated with a mean and standard deviation identical to the acquired vascular channel. A second set of two images(507x507 x&y, 300-400 um z) from two Fischer rats with Alexa680-dextran label in the plasma; these rats were imaged on the same two-photon fluorescence microscope, but with galvano scanners (instead of resonant scanners). A second channel of random Gaussian noise was also added here. Finally, an image of vasculature from a ex-vivo cleared mouse brain (1665x1205x780 um) imaged on a light sheet fluorescence microscope (Miltenyi UltraMicroscope Blaze) was also segmented with our model. Lectin-DyLight 649 was used to label the vasculature in this cohort. The Dice Score, Precision, Recall, Hausdorff 95%, and Mean surface distance will be reported for all of these additional image segmentations, upon generation of ground truth images. Finally, examples of the generated segmentation masks are presented in Author response image 1 for visual comparison. Of final note, should the segmentation results on a new data set be unsatisfactory, the methods downstream from segmentation are still applicable and the model can be further fine-tuned on other out-of-distribution data.

Author response image 1.

Examples of the deep learning model output on out of distribution data from a different mouse strain, from a different species (Fischer rat), and on a different microscope using a different imaging modality.

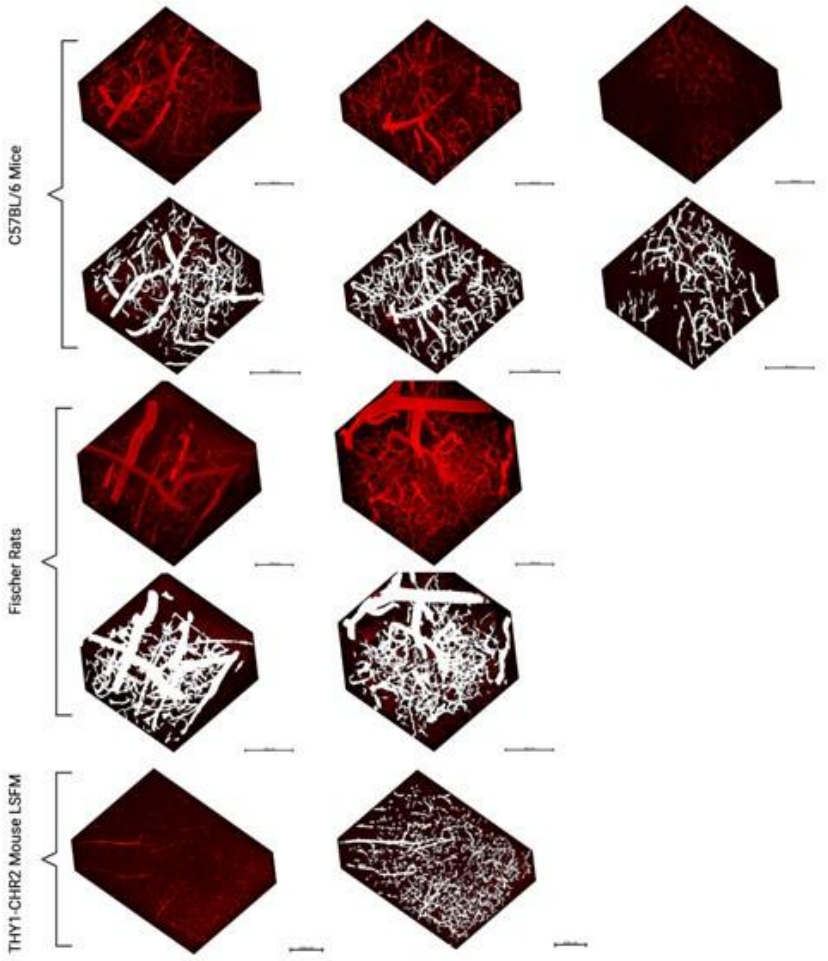

> *(2) Some of the chosen analysis results seem to not fully match the shown data, or the visualization of the data is hard to interpret in the current form.*

We are updating the visualizations to make them more accessible and we will ensure matching between tables and figures.

> *(3) Additionally, some measures seem not fully adapted to the current situation (e.g. the efficiency measure does not consider possible sources or sinks). Thus, some additional analysis work might be required to account for this.*

Thank you for your comment. The efficiency metric was selected as it does not consider sources or sinks. We do agree that accounting for vessel subtypes in the analysis (thus classifying larger vessels as either supplying or draining) would be uniquely useful: notwithstanding, it is extremely laborious. We are therefore leveraging machine learning in a parallel project to afford vessel classification by subtype. The source/sink analysis is also confounded by the small field-of-view of in situ 2PFM. Future work will investigate network remodelling across the whole brain with ex-vivo light sheet fluorescence microscopy.

> *(4) The authors apply their method to in vivo data. However, there are some weaknesses in the design that make it hard to accept many of the conclusions and even to see that the method could yield much useful data with this type of application. Primarily, the acquisition of a large volume of tissue is very slow. In order to obtain a network of vascular activity, large volumes are imaged with high resolution. However, the volumes*

> *are scanned once every 42 seconds following stimulation. Most vascular responses to neuronal activation have come and gone in 42 seconds so each vessel segment is only being sampled at a single time point in the vascular response. So all of the data on diameter changes are impossible to compare since some vessels are sampled during the initial phase of the vascular response, some during the decay, and many probably after it has already returned to baseline. The authors attempt to overcome this by alternating the direction of the scan (from surface to deep and vice versa). But this only provides two sample points along the vascular response curve and so the problem still remains.*

We thank the Reviewer for bringing up this important point.

Although vessels can show relatively rapid responses to perturbation, vascular responses to photostimulation of ChannelRhodopsin-2 in neighbouring neurons are typically long lasting: they do not come and go in 42 seconds. To demonstrate this point, we acquired higher temporal-resolution images of smaller volumes of tissue over 5 minutes preceding and following the 5-s photoactivation with the original parameters. Imaging protocol was different in that we utilized a piezoelectric motor, smaller field of view, and only 3x frame averaging, resulting in a temporal resolution of 1.57-2.63 seconds. This acquisition was repeated at 4 different cortical depths (325 um, 250 um, 150um, and 40 um) in a single mouse.The vascular radii were estimated using our presented pipeline. Raw data and LOESS fits are shown in Author response image 2 (below). Vessels shorter than 20 um in length were excluded from the analysis. A video of one of the acquisitions is shown along with the timecourses of select vessels' caliber changes in Author response image 3. The vascular caliber changes following photostimulation persisted for several minutes, consistent with earlier observations by us and others1–4. These higher temporal-resolution scans of smaller tissue volumes will be repeated in two more mice; we will therein assess the repeatability of individual vessel responses to repeated stimulations.

Author response image 2.

A. The vascular radii of multiple vessels were imaged at 4 different cortical depths, each within a 507 x (75-150) x (30-45)um tissue volume. Baseline scanning lasted for 5 minutes, followed by 5 seconds of blue or green light stimulation at 4.3 mW/mm2, and culminating in 5 minutes of post-stimulation scanning. B. LOESS fits of the vessel radius estimates for each vessel segment identified.

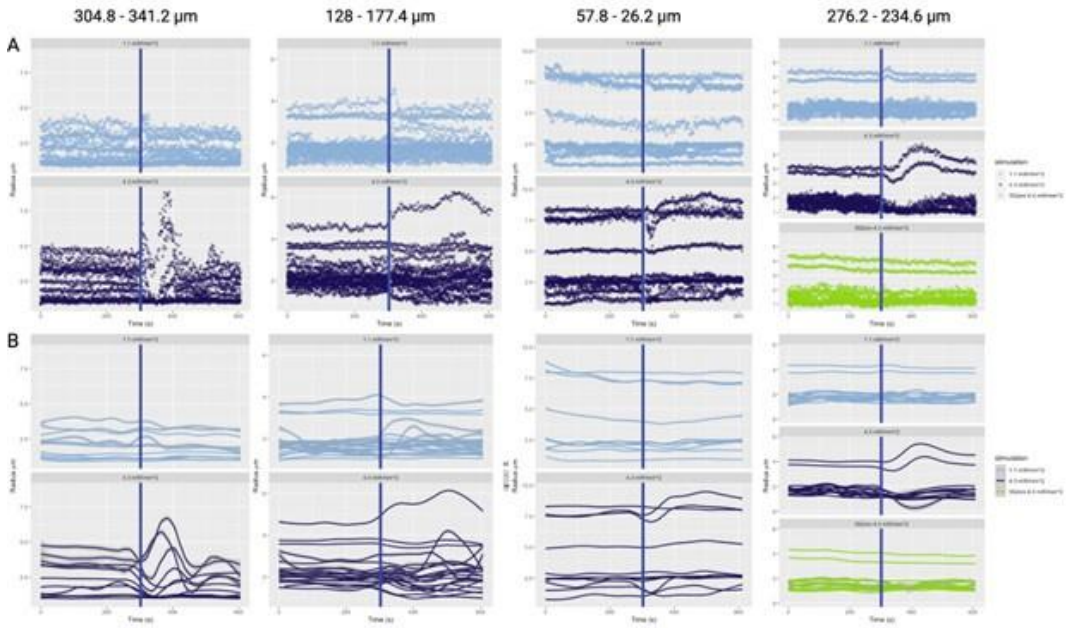

Author response image 3.

Estimated vascular radius at each timepoint for select vessels from the imaging stack shown in the following video: https://flip.com/s/kB1eTwYzwMJE

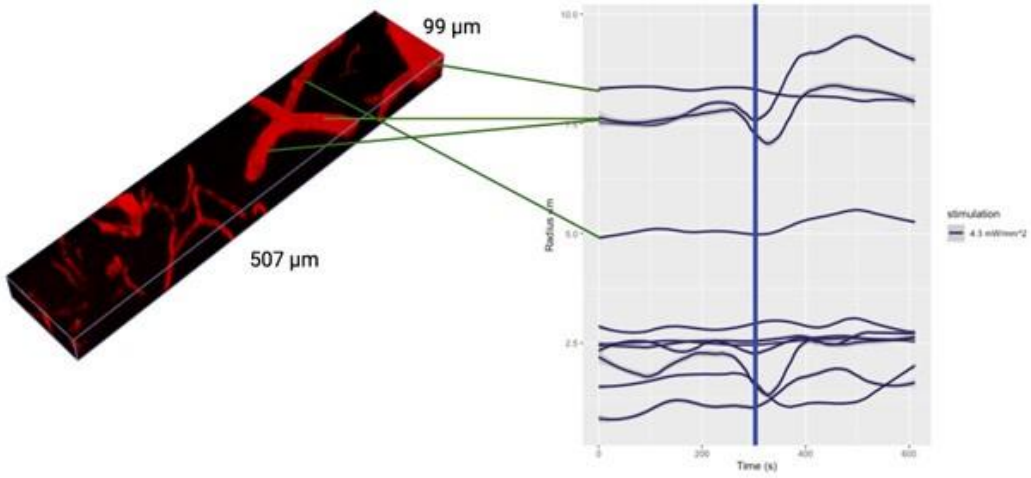

> *(5) A second problem is the use of optogenetic stimulation to activate the tissue. First, it has been shown that blue light itself can increase blood flow (Rungta et al 2017). The authors note the concern about temperature increases but that is not the same issue. The discussion mentions that non-transgenic mice were used to control for this with "data not shown". This is very important data given these earlier reports that have found such effects and so should be included.*

We will update the manuscript to incorporate the data on volumetric scanning in nontransgenic C57BL/6 mice undergoing blue light stimulation, with identical parameters as those used in Thy-ChR2 mice. As before, responders were identified as vessels that following blue light stimulation show a radius change greater than 2 standard deviations of their baseline radius standard deviation: their estimated radii changes are shown in Author

response image 4 below. There were no statistical difference between radii distributions of any of the photostimulation conditions and pre-photostimulation baseline. A comparison of this with the transgenic THY1-ChR2-EYFP mice will be included in manuscript updates.

Author response image 4.

Radius change measurements for responding vessels from the Thy1-ChR2 mice described in the manuscript (top row) vs. 4 wild-type C57BL6/J mice (bottom row). Response to photostimulation was defined as a change above twice their baseline standard deviation. 458nm light was applied at 1.1 mW/mm^2 and 4.3 mW/mm^2; while 552 nm light was applied at 4.3 mW/mm^2. No statistically significant differences were observed between the radii distributions in any condition, Wilcoxon test, Bonferroni correction.

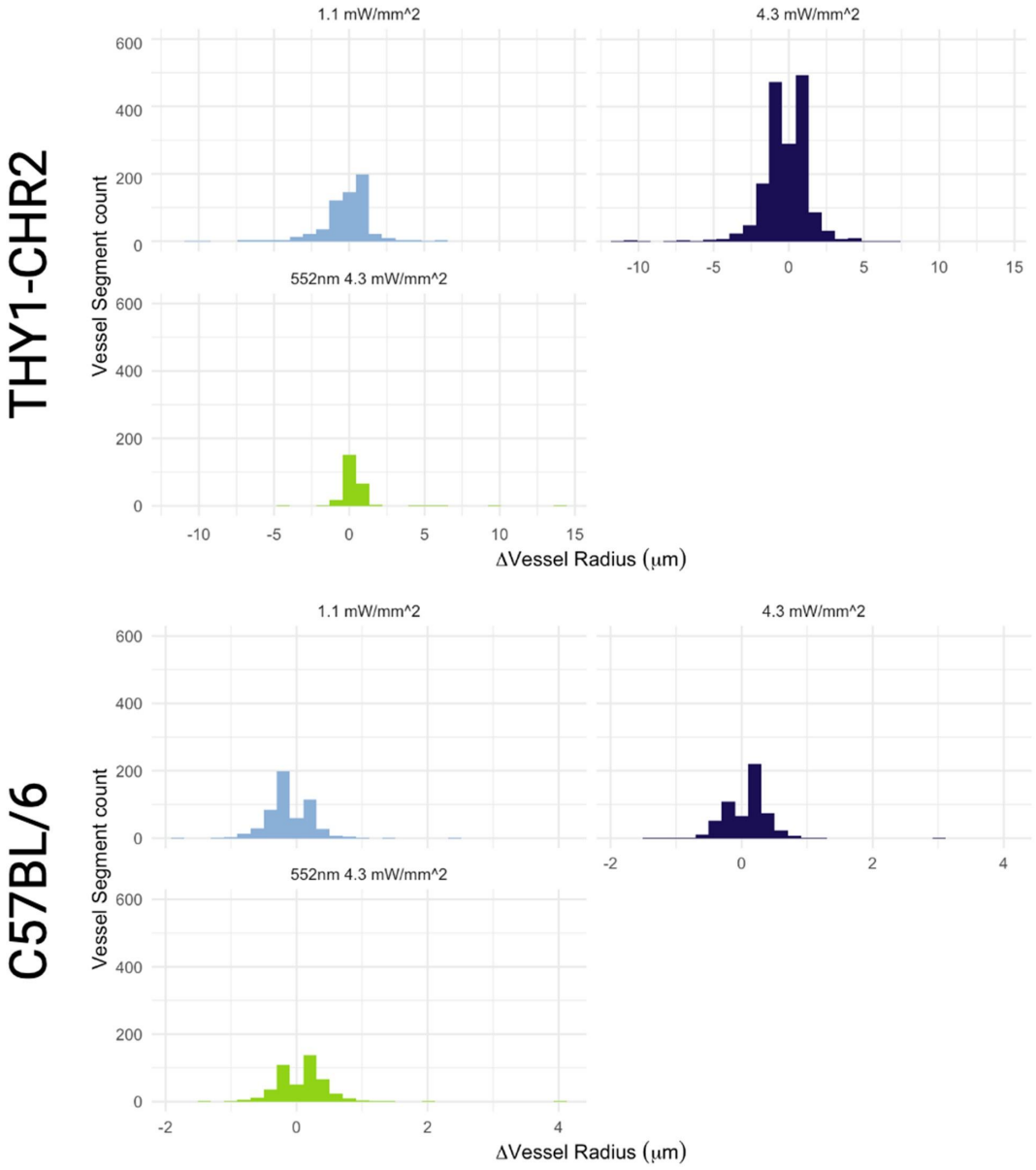

> *(6) Secondly, there doesn't seem to be any monitoring of neural activity following the photo-stimulation. The authors repeatedly mention "activated" neurons and claim that vessel properties change based on distance from "activated" neurons. But I can't find*

> *anything to suggest that they know which neurons were active versus just labeled. Third, the stimulation laser is focused at a single depth plane. Since it is single-photon excitation, there is likely a large volume of activated neurons. But there is no way of knowing the spatial arrangement of neural activity and so again, including this as a factor in the analysis of vascular responses seems unjustified.*

Given the high fidelity of Channel-Rhodpsin2 activation with blue light, we assume that all labeled neurons within the volume of photostimulation are being activated. Depending on their respective connectivities, their postsynaptic neurons (whether or not they are labelled) are also activated. We indeed agree with the reviewer that the spatial distribution of neuronal activation is not well defined. We will revise the manuscript to update the terminology from activated to labeled neurons and stress in the Discussion that the motivation for assessing the distance to the closest labelled neuron as one of our metrics is purely to demonstrate the possibility of linking vascular response to activations in some of their neighbouring neurons and including morphological metrics in the computational pipeline. Of final note, the depth-dependence of the distance between labelled neurons and responding vessels can also readily be assessed using our computational pipeline.

> *(7) The study could also benefit from more clear illustration of the quality of the model's output. It is hard to tell from static images of 3-D volumes how accurate the vessel segmentation is. Perhaps some videos going through the volume with the masks overlaid would provide some clarity. Also, a comparison to commercial vessel segmentation programs would be useful in addition to benchmarking to the ground truth manual data.*

We generated a video demonstrating the deep-learning model outputs and have made the video available here: https://flip.com/s/_XBs4yVxisNs Additional videos will be uploaded.

> *(8) Another useful metric for the model's success would be the reproducibility of the vessel responses. Seeing such a large number of vessels showing constrictions raises some flags and so showing that the model pulled out the same response from the same vessels across multiple repetitions would make such data easier to accept.*

We have generated a figure demonstrating the repeatability of the vascular responses following photoactivation in a volume, and presented them next to the corresponding raw acquisitions for visual inspection. It is important to note that there is a significant biological variability in vessels' responses to repeated stimulation, as described previously 2,5. Constrictions have been reported in the literature by our group and others 1,3,4,6,7, though their prevalence has not been systematically studied to date. Concerning the reproducibility of our analysis, we will demonstrate model reproducibility (as a metric of its success) in the updated manuscript.

Author response image 5.

Registered acquisitions of the vasculature before and after optogenetic stimulation for 5 scan pairs over 3 different stimulation conditions. The estimated radii along vessel segments are presented.

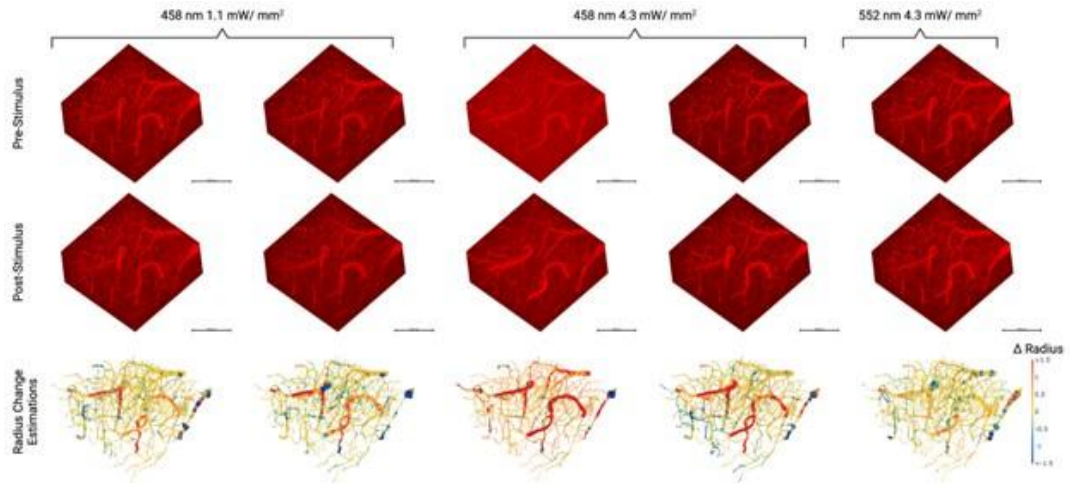

Author response image 6.

Sample capillaries constrictions from maximum intensity projections at repeated timepoints following optogenetic stimulation. Baseline (pre-stimulation) image is shown on the left and the post-stimulation image, on the right, with the estimated radius changes listed to the left.

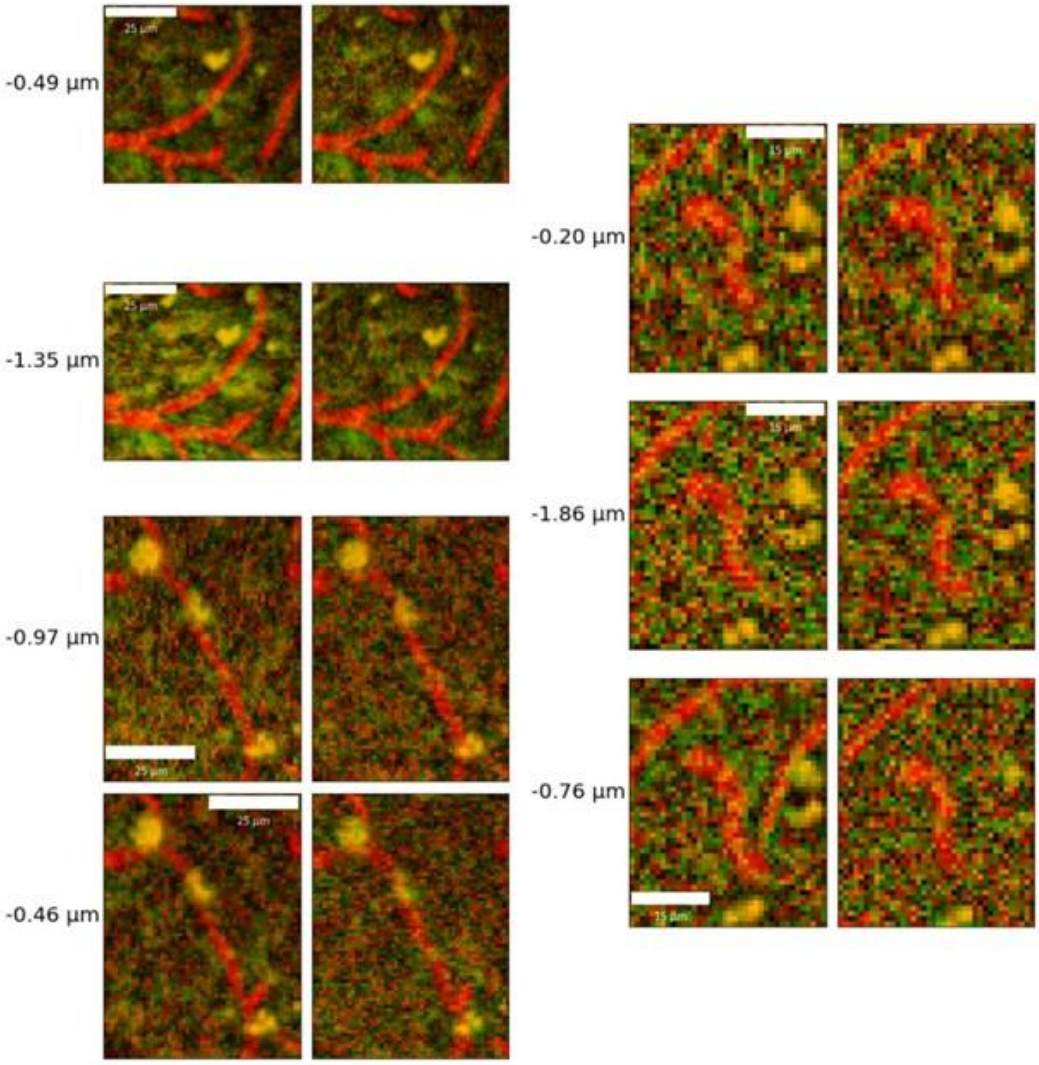

> *(9) A number of findings are questionable, at least in part due to these design properties. There are unrealistically large dilations and constrictions indicated. These are likely due to artifacts of the automated platform. Inspection of these results by eye would help understand what is going on.*

Some of the dilations were indeed large in magnitude. We present select examples of large dilations and constrictions ranging in magnitude from 2.08 to 10.80 um for visual inspection (for reference, average, across vessel and stimuli, magnitude of radius changes were 0.32 +/- 0.54 um). Diameter changes above 5 um were visually inspected.

Author response image 7.

Additional views of diameter changes in maximum intensity projections ranging in magnitude from 2.08 um to 10.80 um.

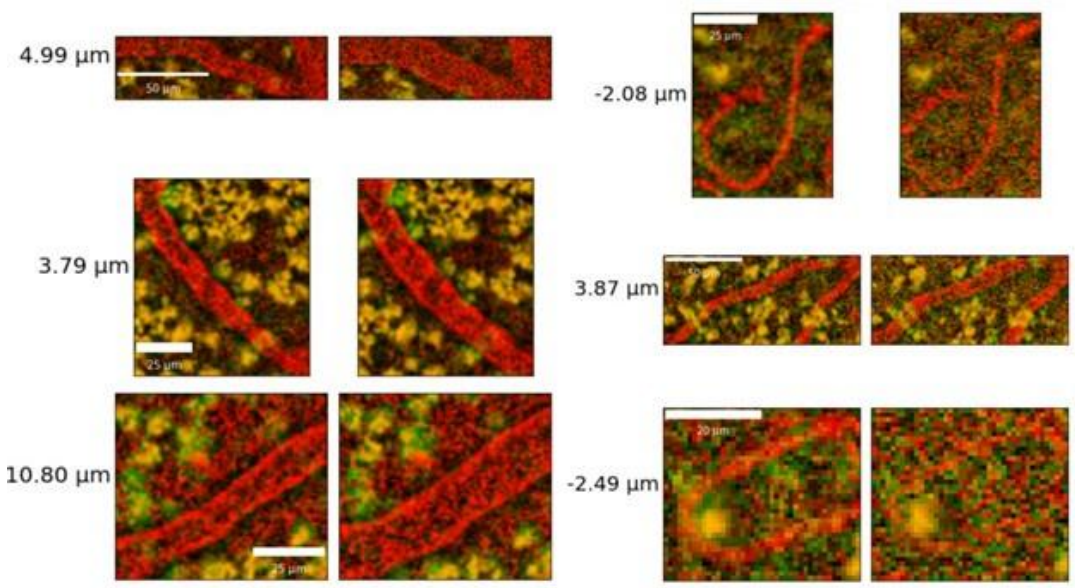

> *(10) In Figure 6, there doesn't seem to be much correlation between vessels with large baseline level changes and vessels with large stimulus-evoked changes. It would be expected that large arteries would have a lot of variability in both conditions and veins much less. There is also not much within-vessel consistency. For instance, the third row shows what looks like a surface vessel constricting to stimulation but a branch coming off of it dilating - this seems biologically unrealistic.*

We now plot photostimulation-elicited vesselwise radius changes vs. their corresponding baseline radius standard deviations (Author response image 8 below). The Pearson correlation between the baseline standard deviation and the radius change was 0.08 ($p<1e-5$) for 552nm 4.3 mW/mm^2 stimulation, -0.08 ($p<1e-5$) for 458nm 1.1 mW/mm^2 stimulation, and -0.04 ($p<1e-5$) for 458nm 4.3 mW/mm^2 stimulation. For non-control (i.e. blue) photostimulation conditions, the change in the radius is thus negatively correlated to the vessel's baseline radius standard deviation. The within-vessel consistency is explicitly evaluated in Figure 8 of the manuscript. As for the instance of a surface vessel constricting while a downstream vessel dilates, it is important to remember that the 2PFM FOV restricts us to imaging a very small portion of the cortical microvascular network (one (among many) daughter vessels showing changes in the opposite direction to the parent vessel is not violating the conservation of mass).

Author response image 8.

A plot of the vessel radius change elicited by photostimulation vs. baseline radius standard deviation.

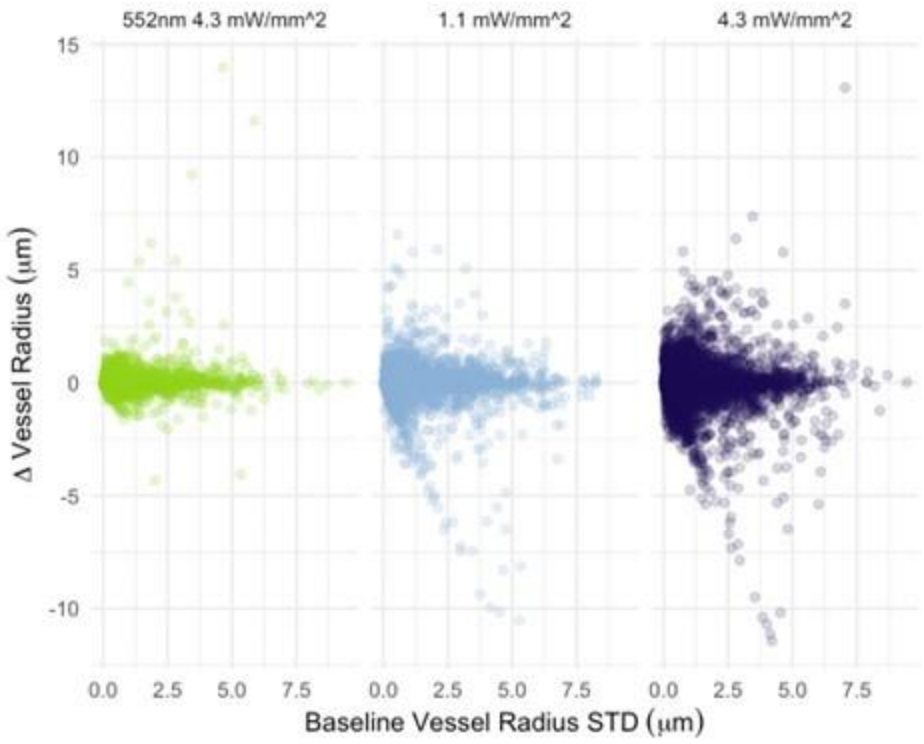

> *(11) As mentioned, the large proportion of constricting capillaries is not something found in the literature. Do these happen at a certain time point following the stimulation? Did the same vessel segments show dilation at times and constriction at other times? In fact, the overall proportion of dilators and constrictors is not given. Are they spatially clustered? The assortativity result implies that there is some clustering, and the theory of blood stealing by active tissue from inactive tissue is cited. However, this theory would imply a region where virtually all vessels are dilating and another region away from the active tissue with constrictions. Was anything that dramatic seen?*

The kinetics of the vascular responses are not accessible via the current imaging protocol and acquired data; however, this computational pipeline can readily be adapted to test hypotheses surrounding the temporal evolution of the vascular responses, as shown in Author response image 2 (with higher temporal-resolution data). Some vessels dilate at some time points and constrict at others as shown in Author response image 2. As listed in Table 2, 4.4% of all vessels constrict and 7.5% dilate for 452nm stimulation at 4.3 mW/mm^2. There was no obvious spatial clustering of dilators or constrictors: we expect such spatial patterns to more likely result from different modes of stimulation and/or in the presence of a pathology. The assortativity peaked at 0.4 (i.e. is quite far from 1 where each vessel's response exactly matches that of its neighbour).

> *(12) Why were nearly all vessels > 5um diameter not responding >2SD above baseline? Did they have highly variable baselines or small responses? Usually, bigger vessels respond strongly to local neural activity.*

In Author response image 9, we now present the stimulation-induced radius changes vs. baseline radius variability across vessels with a radius greater than 5 um. The Pearson correlation between the radius change and the baseline radius standard deviation was 0.04 ($p=0.5$) for 552nm 4.3 mW/mm^2 stimulation, -0.26 ($p<1e-5$) for 458nm 1.1 mW/mm^2 stimulation, and -0.24 ($p<1e-5$) for 458nm 4.3 mW/mm^2 stimulation. We will incorporate an

additional analysis to address this issue by identifying responding vessels as those showing supra-threshold percent change in their radius (instead of SD).

Author response image 9.

A plot of the vessel radius change elicited by photostimulation vs. baseline radius standard deviation in vessels with a baseline radius greater than 5 um.

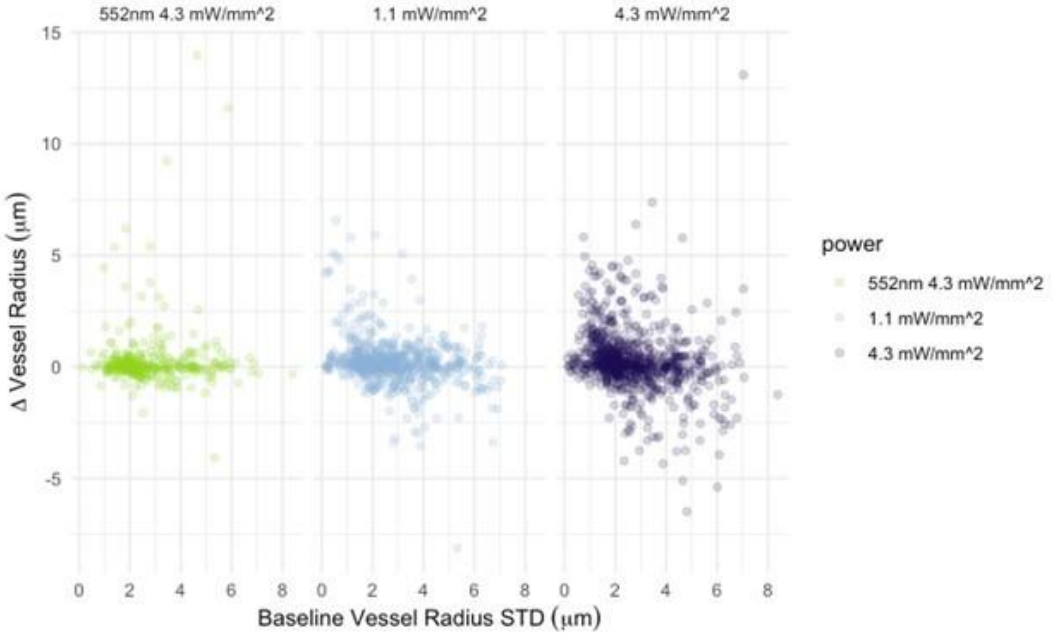

References

(1) Alarcon-Martinez L, Villafranca-Baughman D, Quintero H, et al. Interpericyte tunnelling nanotubes regulate neurovascular coupling. Nature. 2020;kir 2.1(7823):91-95. doi:10.1038/s41586-020-2589-x

(2) Mester JR, Bazzigaluppi P, Weisspapir I, et al. In vivo neurovascular response to focused photoactivation of Channelrhodopsin-2. NeuroImage. 2019;192:135-144. doi:10.1016/j.neuroimage.2019.01.036

(3) O'Herron PJ, Hartmann DA, Xie K, Kara P, Shih AY. 3D optogenetic control of arteriole diameter in vivo. Nelson MT, Calabrese RL, Nelson MT, Devor A, Rungta R, eds. eLife. 2022;11:e72802. doi:10.7554/eLife.72802

(4) Hartmann DA, Berthiaume AA, Grant RI, et al. Brain capillary pericytes exert a substantial but slow influence on blood flow. Nat Neurosci. Published online February 18, 2021:1-13. doi:10.1038/s41593-020-00793-2

(5) Mester JR, Bazzigaluppi P, Dorr A, et al. Attenuation of tonic inhibition prevents chronic neurovascular impairments in a Thy1-ChR2 mouse model of repeated, mild traumatic brain injury. Theranostics. 2021;11(16):7685-7699. doi:10.7150/thno.60190

(6) Mester JR, Rozak MW, Dorr A, Goubran M, Sled JG, Stefanovic B. Network response of brain microvasculature to neuronal stimulation. NeuroImage. 2024;287:120512. doi:10.1016/j.neuroimage.2024.120512

(7) Hall CN, Reynell C, Gesslein B, et al. Capillary pericytes regulate cerebral blood flow in health and disease. Nature. 2014;508(7494):55-60. doi:10.1038/nature13165